Geochronology and geochemistry of felsic xenoliths in lamprophyre dikes from the southeastern margin of the North China Craton: implications for the interleaving of the Dabie–Sulu orogenic crust

Fei Wu, Yilin Xiao, Lijuan Xu, M. Santosh, Shuguang Li, Jian Huang, Zhenhui Hou & Fang Huang

Geochronology and geochemistry of felsic xenoliths in lamprophyre dikes from the southeastern margin of the North China Craton: implications for the interleaving of the Dabie–Sulu orogenic crust

Fei Wu[a], Yilin Xiao[a]*, Lijuan Xu[a], M. Santosh[b,c], Shuguang Li[a], Jian Huang[a], Zhenhui Hou[a] and Fang Huang[a]

[a]*CAS Key Laboratory of Crust-Mantle Materials and Environments, School of Earth and Space Sciences, University of Science and Technology of China, Hefei, China;* [b]*School of Earth Science and Resources, China University of Geosciences, Beijing, PR China;* [c]*Faculty of Science, Kochi University, Kochi, Japan*

Lamprophyre dikes emplaced in a Jurassic granite at the southeastern margin of the North China Craton (NCC) carry different types of xenoliths. Here, we report a combined study of zircon U–Pb ages and whole-rock geochemistry of the xenoliths, as well as an Ar–Ar age of the lamprophyre, providing constraints on the sources of the magmatism and tectonic evolution in the southeastern margin of NCC. Phlogopite from the lamprophyre dike gave a $^{40}Ar/^{39}Ar$ plateau age of 116.15 ± 0.33 Ma. The felsic xenoliths can be classified into three groups: monzogranite, banded biotite granitic gneiss, and garnet-bearing gneiss. The internal structures of zircons from the banded biotite granitic gneiss xenolith show complex growth patterns. The mantles of these zircons display low luminance with a concordant SHRIMP U–Pb age of 227 ± 10 Ma. The rims with lighter luminance provide a SHRIMP U–Pb age of 213 ± 10 Ma, both ages are identical within error and significantly different from the ages of the basement rocks in the surrounding Bengbu uplift. However, the age is identical to those of the ultrahigh-pressure metamorphic rocks in the adjacent Dabie–Sulu orogen. In addition, zircon mantle domains of the banded biotite granitic gneiss xenolith have low Th/U ratios (>0.01) and flat HREE patterns ($(Yb/Dy)n < 10$), which suggest growth in an assemblage with garnet during HP metamorphism. The rim domains show very low Th/U ratios (<0.01) and steep HREE patterns ($(Yb/Dy)n > 10$), implying growth during exhumation in the absence of a garnet. Our studies show that the banded biotite gneiss represents vestiges of the subducted South China crust injected into or thrust below the North China Craton and provides constraints on the process of underthrusting in a continental collision zone, as well as the Mesozoic tectonic history of the southeastern margin of the NCC.

Keywords: xenolith; North China Craton; geochemistry; zircon; continental collision

1. Introduction

The geodynamics of continental collision zones reveal thickening in the orogenic crust and in the underlying lithosphere. The crust in continent collision zones which have low density and low temperature has a different fate compared with that in oceanic subduction zones. The Dabie–Sulu orogen is one of the largest ultrahigh pressure (UHP) metamorphic belts in the world, and formed by Triassic continental collision between the South China Block (SCB) and the North China Craton (NCC), with peak metamorphic ages around 230 Ma (e.g. Li *et al.* 1993, 2000; Jahn *et al.* 1996; Ireland *et al.* 2000; Yang *et al.* 2003; Zheng *et al.* 2009). Post-collisional magmatism is voluminously developed in the Dabie–Sulu orogenic belts and adjacent blocks. Since some post-collisional magmatic rocks occurring along the southeastern margin of the NCC are considered as products of SCB crust melting (e.g. Yang *et al.* 2010; Jiang *et al.* 2012; Li *et al.* 2013), it is possible that some part of the subducted SCB continental crust was emplaced into the adjacent NCC crust.

The Jingshan granitic pluton in the Bengbu uplift area is a typical case of such post-collisional magmatic rocks. It is a Jurassic intrusion that is located in the southeastern margin of the NCC, some 150 km NNE of the Dabie–Sulu UHP metamorphic belt. Previous studies have reported that the Jingshan granite contains abundant Triassic and Neoproterozoic inherited zircons (Xu *et al.* 2005; Yang *et al.* 2010; Wang *et al.* 2011; Li *et al.* 2013; Xu *et al.* 2013), with ages similar to those of zircons from metamorphic rocks in the Dabie–Sulu orogenic belt and the northern SCB margin. In general, Neoproterozoic magmatic events in the SCB are considered to reflect continental growth by magmatism during rifting of the supercontinent Rodinia (Huang *et al.* 2006). A recent study reported extremely low and heterogeneous $\delta^{18}O$ values in the inherited metamorphic zircons from the Jingshan pluton, which are consistent with those in metamorphic zircons from the Dabie–Sulu orogen (Wang *et al.* 2013). These observations suggest that the Jingshan granite was generated from the subducted SCB crust, indicating that the collision and subduction of the

continental crust influenced the lithosphere adjacent to the orogenic belt.

However, the geodynamic setting and the origin of the Jingshan pluton remain equivocal. Yang *et al.* (2010) suggested upwelling of the asthenosphere accompanying delamination of the thickened NCC lithosphere, followed by the southeastward subduction of the SCB beneath the NCC along the Tan-Lu fault zone. The resultant partial melting of the intruded SCB crust generated the Late Jurassic plutons such as the Jingshan leucogranite. Li *et al.* (2013) proposed a 'crustal flow' model to explain the mechanism of SCB intrusion and melting. They suggested that there are partially melted source rocks at depth beneath the Sulu orogen. Thus, crustal injection from the SCB to the NCC could be in the form of crustal flow after the Dabie–Sulu orogen was transected by the Tan-Lu fault during Late Jurassic time. Such crustal injection could have been caused by the E–W lateral pressure gradient triggered by the Late Jurassic topographic gradient (Zhu *et al.* 2009). The felsic melt derived from such a crust ascended and formed the Jingshan granite. The above models were all based on observations of magmatism in the Bengbu area, and no

direct evidence for the composition and structure of the crust in this area has been available.

Here, we report precise zircon U–Pb ages and detailed geochemical data on different types of crustal xenoliths found in a lamprophyre dike in the Jingshan granite, with the purpose of understanding the deep crust in the southeastern NCC margin. Our study suggests that these newly found xenoliths could represent fragments of the underthrusted SCB crust below the southeastern margin of the NCC. These data constrain the crustal properties of the intruded SCB and the mechanism of crustal thickening in the southeastern NCC margin.

2. Geological setting and sample descriptions

The E–W-trending Bengbu uplift area is located in the southeastern margin of the NCC, with the Tan-Lu fault zone on the east and the Hefei basin on the south (Figure 1a). The basement of the Bengbu uplift is composed of the Wuhe complex, which mainly consists of Archaean metamorphic rocks such as garnet-clinopyroxenite, garnet-amphibolite, and supracrustal rocks (Xu
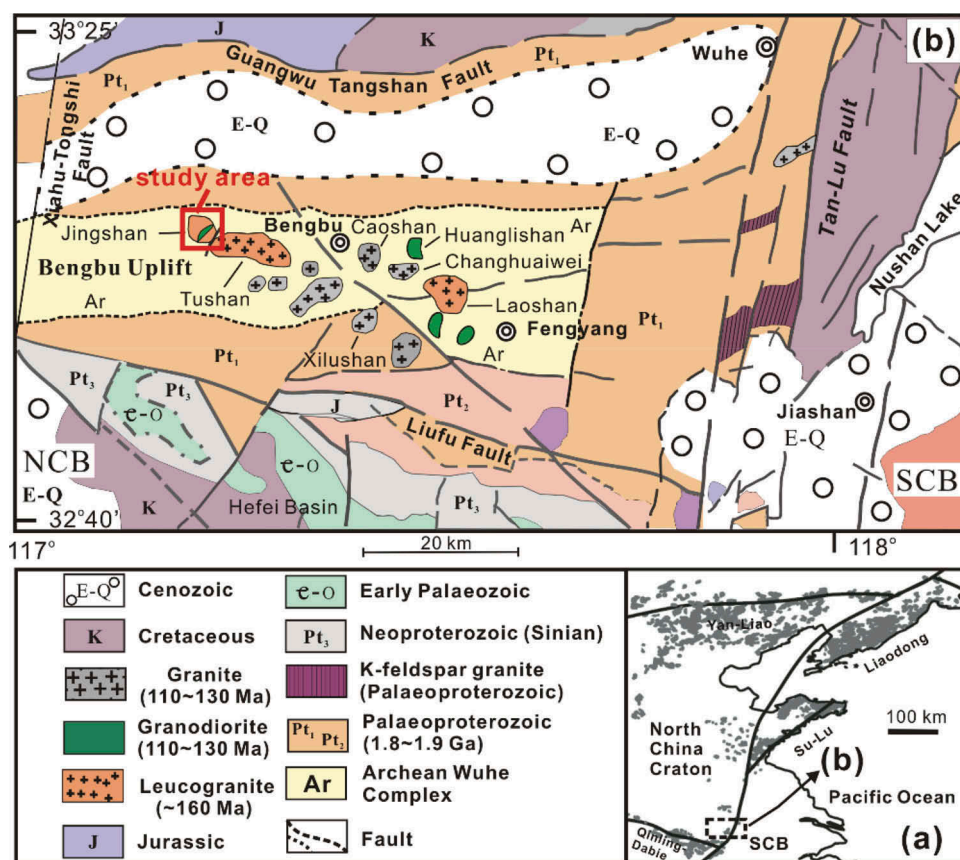
Figure 1. (a) Simplified geological map showing the distribution of Mesozoic igneous rocks in the eastern part of the North China Craton (modified after Yang *et al.* (2008a) and Liu *et al.* (2012)). SCB stands for the South China Block. (b) Detailed geological map showing the locations of Mesozoic granites in the Bengbu uplift (modified after Li *et al.* (2013) and Liu *et al.* (2012)). Location of the study area is marked on the map.

et al. 2006; Guo and Li 2009b; Liu *et al.* 2009). Granitic plutons that intruded into this basement are widespread in the Bengbu uplift area, including biotite-granite, monzogranite, and plagioclase granite. Zircon U–Pb dating indicates that most of these granitic plutons formed in the Late Jurassic (~160 Ma) and Early Cretaceous (130–112 Ma) (Yang *et al.* 2010) periods. The Jingshan granitic pluton (GPS location: 32°57′02′ N 117°11′00′ E, area around 1×10^6 m²) is located in the western part of the Bengbu uplift in Huaiyuan county, Anhui Province (Figure 1b). The garnet-bearing granite is mainly composed of coarse- to medium-grained quartz-rich lithologies with abundant pegmatite and aplite veins. Mafic restites rich in biotite

and garnet are also present (Xu *et al.* 2013). Garnets in the pluton have been interpreted to trace the source and process of crustal melting and subsequent magma evolution (Xu *et al.* 2013). Zircon U–Pb ages show that the garnet-bearing granite intruded the Wuhe metamorphic complex at ~160 Ma (Xu *et al.* 2005; Yang *et al.* 2010). A small number of lamprophyre dikes with various types of crustal xenoliths are found in the Jingshan pluton (Figure 2a), which are the focus of the present study. The lamprophyre dikes intruded the granite in NE–SW directions, and are 0.5–2 m wide and 80–120 m long (Figure 2a and b). The lamprophyre samples are porphyritic with abundant phlogopite, amphibole, and clinopyroxene phenocrysts, and
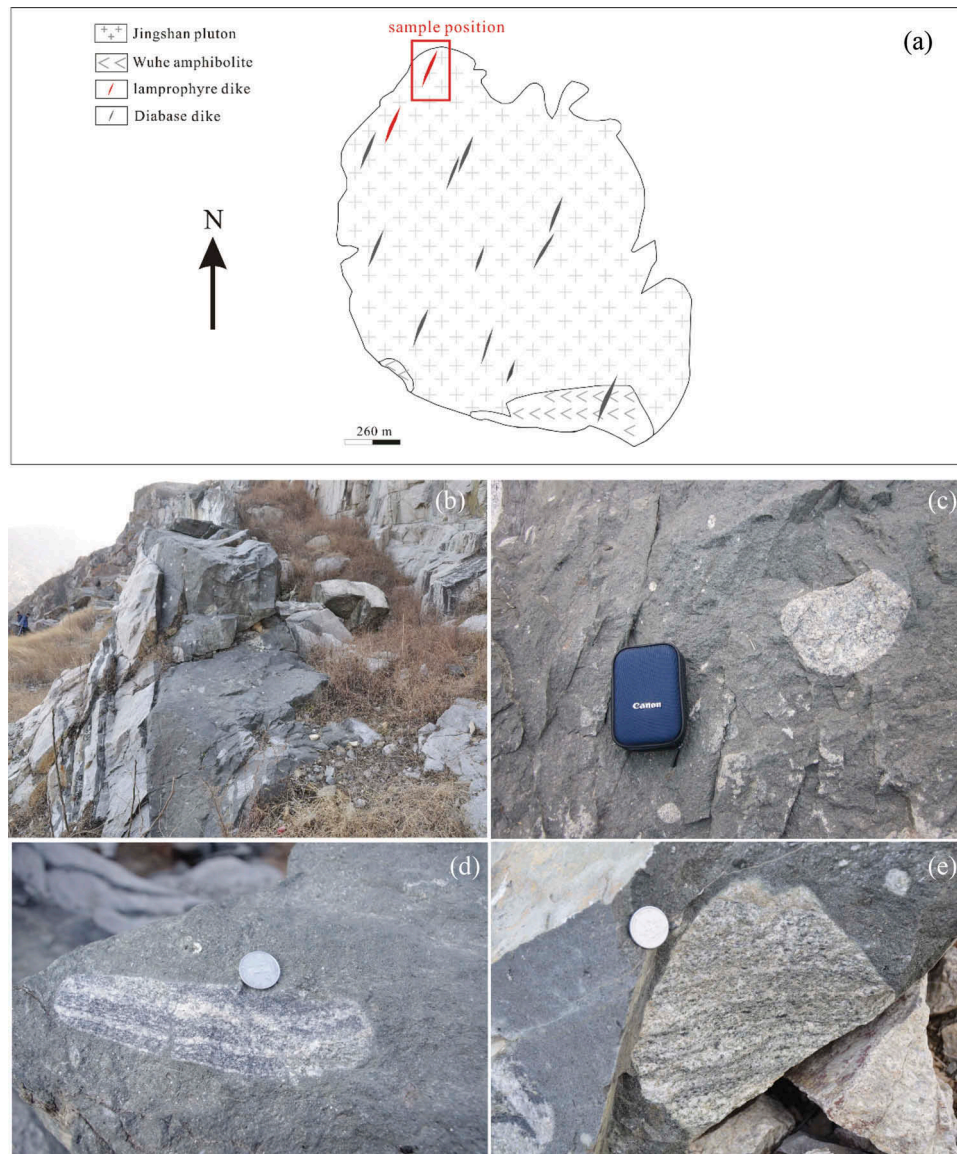
Figure 2. (a) Schematic geological map of the Jingshan pluton (modified after Li *et al.* (2013)), lamprophyre dikes are located in the northeast of the pluton. (b), (c), (d) and (e) Field photographs of lamprophyre dikes and the xenoliths entrained in them in the Jingshan granite. (b) The Jingshan granite and intruded lamprophyre dikes. (c) Monzogranite xenolith. (d) Banded biotite granitic gneiss xenolith. (e) Garnet-bearing plagioclase gneiss xenolith.

fine-grained biotite, clinopyroxene, plagioclase, and alkali feldspar in the matrix. The crustal xenoliths collected from the lamprophyre dikes range from 4 to 20 cm in diameter and most have a round shape without sharp boundaries (Figure 2c–e). Based on petrological observations, the xenoliths in the lamprophyre dikes can be divided into three types: (1) monzogranite xenoliths showing a massive granular texture and composed of medium- and coarse-grained K-feldspar, plagioclase, quartz, and minor biotite (Figure 2c); (2) banded biotite granitic gneiss xenoliths composed of biotite, alkali feldspar, plagioclase, and quartz, with accessory zircon, titanite, apatite, and magnetite (Figure 2d); and (3) garnet-bearing plagioclase gneiss xenoliths dominated by biotite, plagioclase, quartz, and minor garnet (Figure 2e).

3. Analytical methods

3.1. Whole-rock major and trace elements

Fresh rock samples were powdered to <200 μm. Bulk major elements were measured by X-ray fluorescence (XRF) at the Instruments Centre for Physical Science, University of Science and Technology of China, Hefei (USTC). Analytical uncertainties of major elements were better than 2%. Bulk trace elements were analysed from solution after acid digestion by ICP-MS. About 50 mg of powders were acid-digested in pressure vessels and transferred to diluted HNO_3, ensuring that the powders were totally dissolved. Solution measurements were conducted on the Elan 6100 DRC ICP-MS at the CAS Key Laboratory of Crust–Mantle Materials and Environments, University of Science and Technology of China, Hefei (USTC). Detailed analytical procedures were described in Hou and Wang (2007). The reproducibility was better than 5% for elements with concentrations >10 ppm and less than 10% for those <10 ppm monitored by USGS standard materials.

3.2. LA-ICP-MS in situ zircon trace elements

In situ trace element analysis of zircon grains was performed by LA (laser ablation)-ICP-MS (Iizuka and Hirata 2004) (Perkin Elmer ELAN DRC II) at the CAS Key Laboratory of Crust–Mantle Materials and Environments, University of Science and Technology of China, Hefei (USTC). Before laser ablation, zircon cathodoluminescence images (CL images) were taken for selecting analytical spots. The sizes of the laser ablation spots range from 44 μm to 60 μm, depending on the sizes of the zircon grains. NIST 610 glass was analysed between every eight measurements as a standard for zircon trace element calibration, with working values recommended by Pearce et al. (1997). The uncertainty of trace element analysis of our measurements is less than 10% (2σ).

3.3. LA-ICP-MS zircon U-Pb dating

U–Pb dating for zircons was carried out by LA-ICP-MS (Perkin Elmer ELAN DRC II) at the CAS Key Laboratory of Crust–Mantle Materials and Environments, USTC. The spot size of laser ablation ranges from 44 μm to 60 μm. Zircon 91500 standard (Wiedenbeck et al. 1995) was analysed between every five unknown measurements. The $^{238}U/^{206}Pb$, $^{235}U/^{207}Pb$, and $^{232}Th/^{208}Pb$ ratios of the spot analysed were calibrated to reference zircon 91500, following the procedures outlined in the work of Gu et al. (2013) and Xu et al. (2013). Data treatment and common Pb correction were performed by the Excel program ComPbCorr (Andersen 2002). The U–Pb concordia line and weighted mean $^{206}Pb/^{238}U$ ages were calculated using the ISOPLOT program (Ludwig 2001).

3.4. SHRIMP U–Pb zircon U–Pb dating

Zircon was separated and mounted in epoxy, together with standard TEM for zircon SHRIMP U–Pb dating (417 Ma) (Black et al. 2003) and then polished until most zircon grains were approximately cut into half. The U–Pb measurements were performed using a SHRIMP II at the Beijing SHRIMP Centre, following the procedures described by Williams (1998). The spot size for analysis was about 30 μm. ^{204}Pb was measured for common Pb corrections during all the analyses. Uncertainties in ages are quoted at the 95% confidence level (2δ). The U–Pb concordia line and weighted mean $^{206}Pb/^{238}U$ ages calculated using the ISOPLOT program (Ludwig 2001) were used to discuss ages of the rocks.

3.5. $^{40}Ar/^{39}Ar$ isotopic analysis for phlogopite

Coarse-grained phlogopite (up to 1 cm in diameter) from a lamprophyre sample was picked out for $^{40}Ar/^{39}Ar$ age measurement in order to date the formation time of the dike. The $^{40}Ar/^{39}Ar$ dating was carried out at the UW-Madison Rare Gas Geochronology Laboratory, USA. Details of the analytical procedures, including mass spectrometry, procedural blanks, reactor corrections, and estimation of uncertainties, are described by Smith et al. (2008). All ages are shown with ±2σ analytical uncertainties.

4. Results

4.1. Bulk chemical compositions of lamprophyre dikes and the xenoliths

4.1.1. Lamprophyres

Chemical compositions of the Jingshan lamprophyre dikes and their xenoliths are listed in Table 1. The lamprophyres have SiO_2 content from 42.5 to 47.3 wt%. They are enriched in total alkali ($K_2O + Na_2O$ = 6.98–7.84 wt%) and belong to calc-alkaline lamprophyre according to the

Table 1. Compositions of major oxides and trace elements of Jingshan lamprophyre dikes and xenoliths from lamprophyre dikes.

	Lamprophyre dikes					Xenolith I		Xenolith II				Xenolith III	
Sample	13HJS-1-1	13HJS-1-2	13HJS-1-3	13HJS-1-4	11-JS-lam	0905-JS-I-1	0905-JS-I-2	0905JSX-II-1	0905JS-II-2	09JS-10	1106JS-X1	0905-JS-III-1	0905-JS-III-2
SiO_2	42.5	46.2	46	45.4	47.27	65.42	65.92	72.63	69.18	71.49	70.64	68.97	68.18
Al_2O_3	12.3	12.75	12.75	12.7	16.61	15.81	16.08	13.39	14.50	13.20	13.56	14.53	14.74
TiO_2	0.91	1	1.01	0.99	0.87	0.25	0.23	0.36	0.37	0.30	0.58	0.55	0.51
Fe_2O_3	7.63	7.85	8.06	7.85	6.57	1.77	2.22	2.34	2.70	2.08	2.50	2.29	2.77
CaO	10.4	9.7	9.61	10.35	9.53	2.59	2.70	2.21	2.40	1.67	2.28	2.41	2.22
MgO	8.04	9.46	9.44	9.23	9.54	1.18	1.13	1.13	1.25	0.70	0.85	0.85	0.84
K_2O	5.74	4.98	5.14	5.08	4.99	4.32	4.64	2.67	2.78	1.36	3.08	2.65	2.74
Na_2O	2.03	2.47	2.59	2.32	1.99	5.09	5.50	4.78	5.46	7.08	4.14	5.90	6.42
MnO	0.12	0.13	0.15	0.16	0.13	0.05	0.05	0.05	0.06	0.05	0.06	0.06	0.07
P_2O_s	1.25	1.37	1.38	1.4	1.40	0.29	0.31	0.12	0.12	0.05	0.23	0.15	0.16
Total	90.92	95.91	96.13	95.48	98.90	96.77	98.78	99.68	98.82	97.98	97.92	98.36	98.65
A/CNK						0.89	0.85	0.91	0.89	0.82	0.95	0.86	0.84
Na + K						9.41	10.14	7.45	8.24	8.44	7.22	8.55	9.16
Mg#	67.82	70.68	70.08	70.16	74.39	57.14	50.45	49.13	48.08	40.23	40.48	42.61	37.75
Trace element (ppm)													
Li					33.60	4.30	3.72	5.11	5.00	1.83	2.16	3.53	3.30
Be					2.48	4.63	3.47	1.67	1.66	2.52	1.31	1.97	1.67
Sc					12.00	4.95	3.40	4.45	6.14	3.30	8.25	7.25	8.15
V	179	187	186	177	430.00	32.8	19.6	24.20	55.90	9.96	12.50	32.1	19.0
Cr	390	440	430	390	425.00	17.3	18.7	23.90	18.30	9.07	11.80	14.0	17.8
Co					67.90	3.65	6.49	3.93	4.81	1.82	2.31	5.33	3.12
Ni					197.00	20.2	19.9	12.50	9.91	5.99	8.88	6.94	11.3
Cu					49.00	8.42	18.0	33.80	23.80	18.00	14.10	25.3	25.5
Zn					136.00	22.4	177	144.00	24.90	39.90	69.90	30.2	63.5
Ga	16.4	15.5	15.3	14.2	15.60	15.2	15.6	13.90	15.50	18.00	15.10	17.0	19.1
Rb	229	149	151.5	134.5	143.00	40.2	35.3	20.10	22.60	57.20	29.20	31.8	30.6
Sr	1255	1910	1725	1935	1603	1220	1289	429.00	448.00	265.0	435.00	319	343
Y	34.6	33.8	32.6	31.4	35.10	15.3	17.2	11.50	11.10	26.90	22.20	34.4	39.5
Zr	383	340	326	312	307.00	227	230	105.00	102.00	207.0	284.0	326	226
Nb	20	17.2	17	16	16.20	9.14	9.41	8.56	9.01	24.90	9.32	17.7	19.1
Cs	5.46	3.4	3.51	3.2	3.14	0.62	0.55	0.73	0.74	0.35	0.43	0.54	0.49
Ba	3490	4640	4320	4800	3511	4962	4441	1857	1686	651.0	1784	1660	1760
La	153	161	154.5	151	147	46.9	46.4	35.40	31.90	54.70	39.20	43.9	41.3
Ce	281	298	289	280	203.0	85.6	86.8	62.60	59.00	105.0	74.60	82.6	81.3
Pr	30.3	32.2	32	30.1	33.20	9.51	10.1	7.41	6.30	12.00	9.11	9.86	10.0
Nd	114	122	122	115	124.00	36.3	35.2	26.50	24.10	39.90	33.90	39.8	37.1
Sm	17.95	18.75	18.8	17.55	21.20	5.63	5.71	4.57	3.96	7.48	6.34	7.46	7.43
Eu	4.71	4.94	4.98	4.7	5.51	1.99	1.79	0.99	0.92	0.44	1.62	1.85	1.82
Gd	12.3	12.55	13.15	12.15	15.90	4.65	4.42	3.47	3.21	6.25	5.48	6.61	6.53
Tb	1.45	1.47	1.47	1.42	1.80	0.55	0.55	0.47	0.38	0.94	0.78	0.98	1.02
Dy	6.91	6.74	6.7	6.5	8.60	2.80	2.95	2.61	2.03	5.21	4.57	5.81	6.24

(*Continued*)

Table 1.　(Continued).

Sample	Lamprophyre dikes					Xenolith I		Xenolith II				Xenolith III	
	13HJS-1-1	13HJS-1-2	13HJS-1-3	13HJS-1-4	11-JS-lam	0905-JS-I-1	0905-JS-I-2	0905JSX-II-1	0905JS-II-2	09JS-10	1106JS-X1	0905-JS-III-1	0905-JS-III-2
Ho	1.22	1.16	1.18	1.13	1.33	0.51	0.52	0.47	0.37	0.90	0.87	1.17	1.23
Er	3.03	2.83	2.86	2.78	3.40	1.49	1.44	1.33	1.09	2.27	2.38	3.45	3.51
Tm	0.42	0.4	0.39	0.39	0.46	0.21	0.22	0.20	0.16	0.33	0.36	0.54	0.56
Yb	2.72	2.37	2.25	2.25	2.87	1.43	1.43	1.39	1.10	2.04	2.34	3.59	3.73
Lu	0.43	0.37	0.36	0.37	0.42	0.22	0.21	0.22	0.18	0.29	0.37	0.53	0.55
Hf	8	7.4	7.2	6.7	8.79	6.20	6.11	3.66	2.55	6.83	8.59	7.93	7.27
Ta	0.9	0.8	0.8	0.7	0.72	0.37	0.30	0.57	0.54	0.81	0.30	1.13	0.97
Pb					22.40	66.2	68.9	21.50	14.80	20.30	21.90	23.2	23.8
Th	17.5	16.6	16.6	15.15	20.20	16.8	16.4	8.35	5.91	22.00	9.64	9.36	8.88
U	5	3.67	4.8	3.74	4.60	2.15	2.03	2.34	1.73	4.66	1.02	1.60	1.51

Note: Xenolith I denotes the monzogranite xenolith. Xenolith II denotes the banded biotite granitic gneiss xenolith. Xenolith III denotes the garnet-bearing plagioclase gneiss xenolith.

Figure 3.　$K_2O + Na_2O$ vs. SiO_2 diagram for lamprophyre and xenoliths in Jingshan. Classifications are after Le Bas et al. (1986). The dark curve represents the boundary of alkaline and tholeiite series. Xenolith I denotes the monzogranite xenolith. Xenolith II denotes the banded biotite granitic gneiss xenolith. Xenolith III denotes the garnet-bearing plagioclase gneiss xenolith.
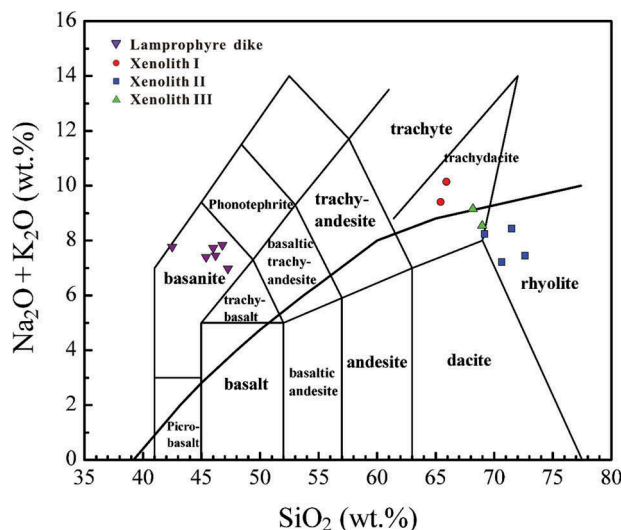
classification of Le Bas et al. (1986) in a $K_2O + Na_2O$ vs. SiO_2 diagram (Figure 3). Moreover, since the main phenocryst minerals of the lamprophyre rocks are phlogopite, and the felsic minerals in groundmass have more alkali feldspar than plagioclase, they are classified as minette following the work of Rock (1987).

The chondrite-normalized REE patterns of the Jingshan lamprophyre exhibit significant enrichment of LREEs relative to HREEs with LREE abundances >200 times and HREE <20 times chondrite (Figure 4b). They also exhibit slightly negative Eu anomalies with Eu/Eu* of 0.92–0.94. In the primitive mantle-normalized trace element diagrams (Figure 4a), these rocks show significant enrichment in LILEs (K, Rb, Ba, Pb, Th, and U), and depletion in HFSEs (Nb, Ta, Zr, Hf, and Ti) (Figure 4a). These trace element signatures are distinct from the diabase dikes from the Bengbu uplift (Liu et al. 2012), which do not show such strong enrichments of LILEs and LREEs.

4.1.2.　Monzogranite xenoliths

Monzogranite xenoliths have ~65 wt% SiO_2, ~1.10 wt% MgO, and ~2.60 wt% CaO (Table 1), and show relatively high Al_2O_3 contents compared to the other xenoliths (~16.0 wt%) and display high total alkali ($K_2O + Na_2O$ = 9.41 and 10.14 wt%). Accordingly, the xenoliths fall into the trachydacite field in a diagram (Figure 3) of total alkali vs. SiO_2 (Le Bas et al. 1986).

The monzogranite xenoliths are enriched in LREEs relative to HREE and exhibit positive Eu anomalies (Eu/
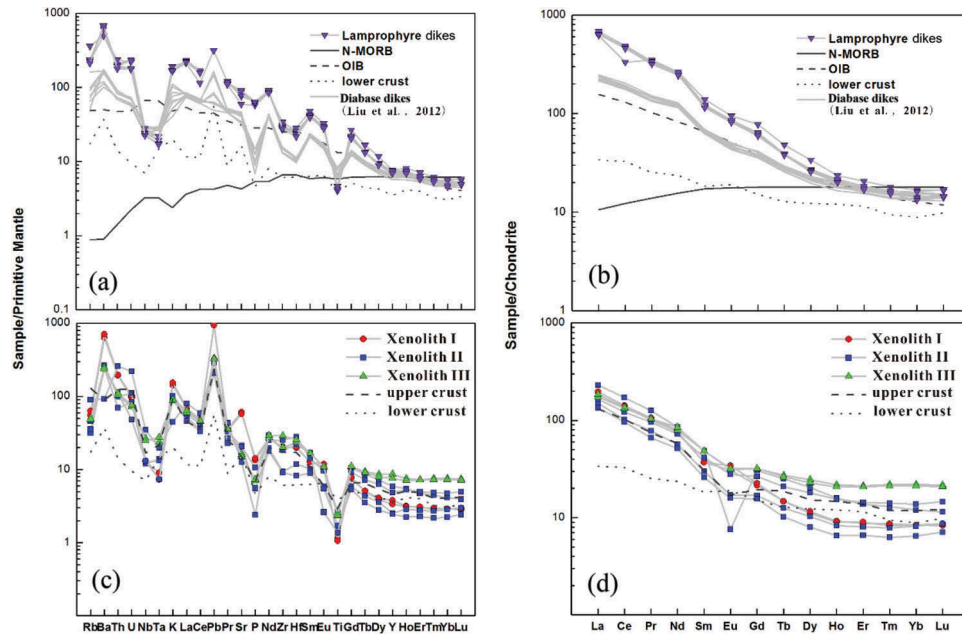
Figure 4. Primitive mantle-normalized trace element patterns (a and c) and chondrite-normalized rare earth element (REE) patterns for lamprophyre dikes and xenoliths from lamprophyre dikes in Jingshan granite. Xenolith I denotes the monzogranite xenolith. Xenolith II denotes the banded biotite granitic gneiss xenolith. Xenolith III denotes garnet-bearing plagioclase gneiss xenolith. The data of Mesozoic diabase dikes from the Bengbu area are from Liu *et al.* (2012). Compositions of chondrite, primitive mantle, N-MORB, and OIB are from Sun and McDonough (1989). The upper crust and the lower crust are from Rudnick and Gao (2003).

Eu* = 1.1; Figure 4c and d). They show significant enrichment in LILEs and Sr, but relative depletion in HFSEs (Nb, Ta, and Ti), as depicted in the primitive mantle-normalized trace element diagrams (Figure 4c).

4.1.3. Banded biotite granitic gneiss xenoliths

Banded biotite granitic gneiss xenoliths have SiO_2 contents ranging from 69.0 to 72.6 wt%, with high contents of MgO (0.70 to 1.25 wt%) and CaO (1.67 to 2.40 wt%) but low contents of Al_2O_3 (13.2 to 13.6 wt%; Table 1). They are enriched in total alkali, with $K_2O + Na_2O$ = 7.22–8.44 wt%, and fall into the rhyolite field in a diagram of total alkali vs. SiO_2 (Le Bas *et al.* 1986; Fig. 3). A/CNK ratios [mole Al/(Na + K + Ca)] range from 0.8 to 1.0, corresponding to metaluminous granites.

Chondrite-normalized REE patterns of the banded biotite granitic gneiss xenoliths (Figure 4) show enrichments in LREEs, with steep LREE and flat HREE patterns. Negative Eu anomalies are indicated by Eu/Eu* ratios of 0.20–0.84. In the primitive mantle-normalized trace element patterns (Figure 4), the xenoliths show evolved compositions with significant enrichment in LILEs, but relative depletion in HFSEs (Nb, Ta, and Ti), Sr, and P.

4.1.4. Garnet-bearing gneiss xenoliths

The garnet-bearing gneissic xenoliths show SiO_2 contents of about 68.5 wt%, MgO contents of about 1.10 wt%, and CaO

contents of about 2.60 wt%, with high contents of Al_2O_3 (about 14.5 wt%) and enriched total alkali contents ($K_2O + Na_2O$ = 8.55–9.16 wt%; Table 1). They fall into the field of rhyolite to trachydacite according to the $K_2O + Na_2O$ vs. SiO_2 classification scheme of Le Bas *et al.* (1986) (Figure 3).

The garnet-bearing gneissic xenoliths are enriched in LREEs relative to HREEs but have flat HREE patterns (Figure 4d). Slightly negative Eu anomalies are indicated by Eu/Eu* ratios of about 0.8. Trace element patterns (Figure 4c) show significant enrichment in LILEs, but relative depletion in HFSEs (Nb, Ta, and Ti) and P.

4.2. $^{40}Ar/^{39}Ar$ age of lamprophyre dikes

$^{40}Ar/^{39}Ar$ isotopic data of phlogopite from the lamprophyre dikes are presented in Table 2. The $^{40}Ar/^{39}Ar$ spectra (Figure 5) gave concordant ages of 116.15 ± 0.33 Ma from the $^{40}Ar/^{39}Ar$ plateau and an identical isochrone age of 116.17 ± 0.34 Ma. The isochron also defines an initial $^{40}Ar/^{39}Ar$ ratio of 294.6 ± 3.1 (2σ), which is within the error of the atmospheric value (295.5). This implies that the effect of excess argon on the obtained plateau age is insignificant.

4.3. Zircon geochronology of the xenoliths

4.3.1. Monzogranites

Zircon grains from the monzogranite xenoliths are euhedral to subhedral, long prismatic, colourless and

Table 2. Ar–Ar isotopic results of Jingshan lamprophyre dikes.

^{36}Ar	1 s	^{37}Ar	1 s	^{38}Ar	1 s	^{39}Ar	1 s	^{40}Ar	1 s	Age ± 2 s (Ma)
0.000015	0.000004	0.000004	0.000006	0.000007	0.000007	0.000021	0.000020	0.003641	0.000068	76.37 ± 50.73
0.000012	0.000004	0.000004	0.000006	0.000007	0.000007	0.000016	0.000020	0.003507	0.000068	76.07 ± 71.22
0.000012	0.000004	0.000004	0.000006	0.000006	0.000007	0.000011	0.000020	0.003397	0.000068	114.91 ± 11.27
0.000013	0.000004	0.000004	0.000006	0.000006	0.000007	0.000012	0.000020	0.003379	0.000068	117.58 ± 2.92
0.000015	0.000004	0.000004	0.000006	0.000006	0.000007	0.000017	0.000020	0.003394	0.000068	115.38 ± 3.44
0.000016	0.000004	0.000004	0.000006	0.000006	0.000007	0.000022	0.000020	0.003416	0.000068	116.37 ± 3.48
0.000017	0.000004	0.000004	0.000006	0.000006	0.000007	0.000032	0.000020	0.003456	0.000068	116.82 ± 1.05
0.000017	0.000004	0.000004	0.000006	0.000005	0.000007	0.000039	0.000020	0.003475	0.000068	116.56 ± 0.55
0.000016	0.000004	0.000004	0.000006	0.000005	0.000007	0.000050	0.000020	0.003491	0.000068	115.82 ± 0.38
0.000016	0.000004	0.000004	0.000006	0.000005	0.000007	0.000054	0.000020	0.003490	0.000068	115.91 ± 0.67
0.000014	0.000004	0.000005	0.000006	0.000005	0.000007	0.000057	0.000020	0.003480	0.000068	116.19 ± 0.25
0.000013	0.000004	0.000005	0.000006	0.000005	0.000007	0.000054	0.000020	0.003474	0.000068	115.95 ± 1.97
0.000012	0.000004	0.000005	0.000006	0.000004	0.000007	0.000039	0.000020	0.003485	0.000068	118.78 ± 6.27

transparent. The elongation (length-to-width) ratios range from 2.5 to 5 with lengths of 50 to 200 μm. CL images show most zircon grains with oscillatory zoning patterns typical of magmatic growth (Figure 6a). As listed in Table 3, they generally have high Th/U ratios (>0.1), consistent with their magmatic origin. LA-ICP-MS analyses of the zircon grains yielded a weighted mean ^{206}Pb/^{238}U age of 122.8 ± 1.8 Ma (n = 21; MSWD = 2.7) (Figure 6b). Thus, the formation age of this xenolith is ca. 123 Ma.

4.3.2. Banded biotite granitic gneiss

Zircon grains from the banded biotite granitic gneiss xenoliths are subhedral to anhedral, round to short prismatic in shape, and are colourless and transparent with abundant mineral inclusions. The elongation ratios range from 1 to 3 with lengths of 100 to 300 μm. CL imaging shows that they have a complex inner structure (Figure 7). In general, they display core–mantle texture with medium brightness in the CL images, and convoluted and blurred zoning patterns, which imply inheritance from a protolith that has experienced intense metamorphic recrystallization. However, a small number of zircon grains have a core with clear oscillatory zoning, suggesting igneous origin. Some zircons have an unzoned mantle and rim, which are homogeneous in CL. This unzoned mantle shows low luminance with bright luminance at the rim. As illustrated in Figure 7 and Table 4, the SHRIMP zircon U–Pb isotope data define a very imprecise upper-intercept at 766 ± 290 Ma, which is controlled by only one analysis. Most core–mantle domains show discordant ages, with apparent ^{206}Pb/^{238}U ages ranging from 232 Ma to 620 Ma, with highly variable Th/U ranging from 0.01 to 1.

The mantle domains with low luminance have concordant ages ranging from 222 Ma to 233 Ma, with a weighted mean age of 227 ± 7 Ma (MSWD = 0.26, Figure 7b) and Th/U ratios from 0.1 to 0.01. Zircons rims with bright luminance show concordant ages of 209–215 Ma, with a weighted mean age of 213 ± 10 Ma (MSWD = 0.04, Figure 7c) and very low Th/U ratio (<0.01).

The zircon trace element data are listed in Table S1 (see http://dx.doi.org/10.1080/00206814.2015.1009182) and shown in Figure 9. The mantle domains display relatively flat REE patterns with (Yb/Dy)$_N$ < 10, whereas the rim domains show steep REE patterns with (Yb/Dy)$_N$ > 10 (Figure 9b).

4.3.3. Garnet-bearing plagioclase gneiss

Zircons from the garnet-bearing plagioclase gneiss xenoliths are subhedral to anhedral, short prismatic, and generally colourless and transparent. Their elongation ratios range from 1 to 3 with lengths of 150 to 400 μm. CL images reveal that the zircon grains generally have
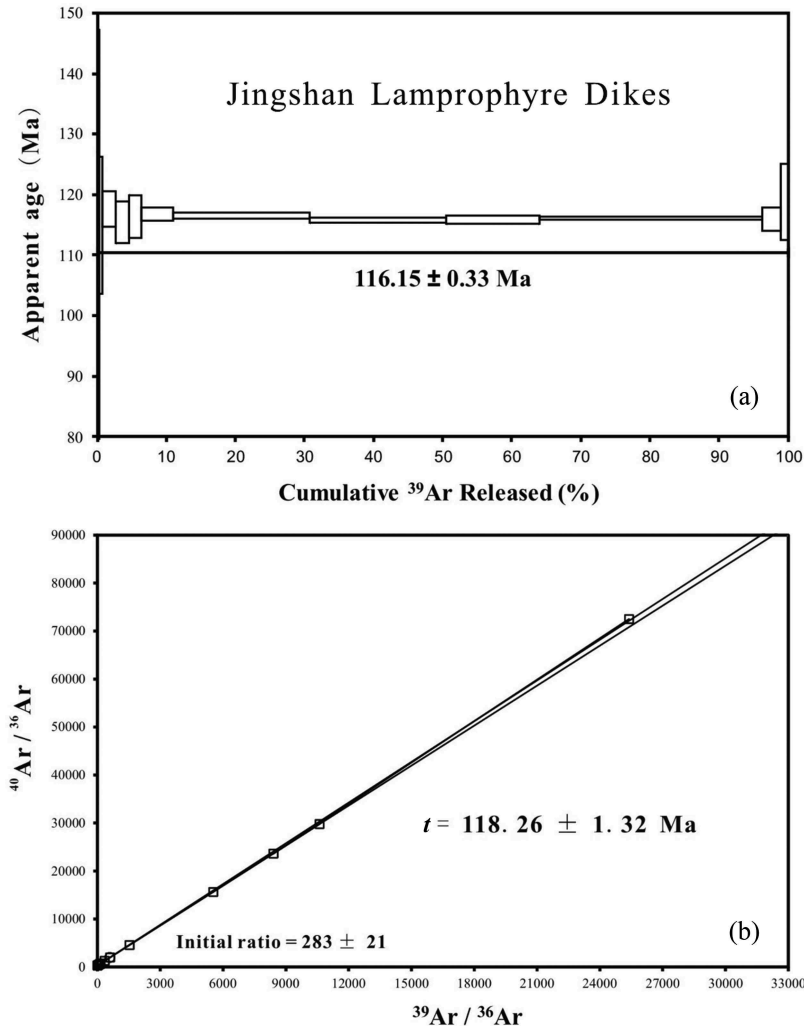
Figure 5. Phlogopite ^{40}Ar–^{39}Ar age spectrum (a) and isochron plots (b) for lamprophyre dikes from Jingshan granite. Data are reported in Table 2.

spherical to multifaceted morphology and internal sector- to fir-tree zoning patterns (Figure 6c). A small number of zircons have cores with weak zoning, and others have unzoned cores that show low luminance (Figure 6d).

SHRIMP U–Pb data are listed in Table 5 and plotted in Figure 6c and d. Two SHRIMP spot analyses of the zircon rims gave ^{206}Pb/^{238}U ages of around 1800 Ma (Figure 6c and d). One SHRIMP spot analyses of the zircon core yielded a ^{206}Pb/^{238}U age of ~2600 Ma (Figure 6d). These old ages represent inherited zircons.

5. Discussion

Previous studies showed that lamproitic rocks from continental collision zones likely formed from decompression melting of metasomatized lithospheric mantle (Guo *et al.* 2004; Gao *et al.* 2007), and we also favour this interpretation. However, given the Ar–Ar age of 116 Ma for the emplacement of the dike, the melting event recorded by the lamprophyre magmas could thus not have been related to post-collisional events that followed the formation of the Dabie–Sulu orogen at 240–225 Ma. Also, there is a significant age gap of >50 Ma between the host Jingshan granite (ca. 160 Ma) and the dikes, making a genetic link unlikely. However, the lamprophyres follow closely in time and are likely related to Cretaceous granitic and granodioritic plutons in the Bengbu area with ages of ~120 Ma (Yang *et al.* 2010; Liu *et al.* 2012). Lithospheric melting may have then been triggered by the uplift of the Bengbu area, which has not been previously precisely dated.

5.1. Origin of different xenoliths

Here, we evaluate the origin of the different types of xenoliths based on their diverse compositions (Figure 3) and ages (Figures 6 and 7).
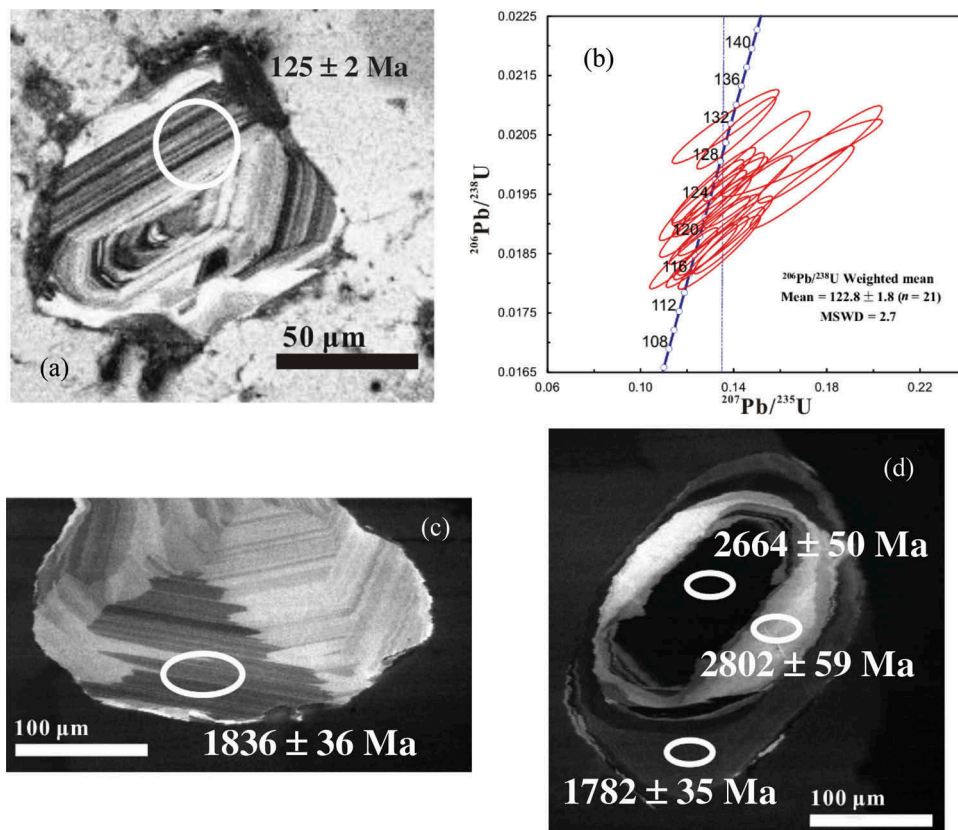
Figure 6. Zircon U–Pb concordia diagrams and CL images for the monzogranite xenolith (a and b) and zircon CL images for garnet-bearing plagioclase gneiss xenoliths (c and d) within lamprophyre dikes in the Jingshan granite: (a) representative CL images of the dated zircon grain from monzogranite xenoliths. (b) Concordant age of the zircon from monzogranite xenoliths. (c) and (d) CL images of the dated zircon grains from garnet-bearing plagioclase gneiss xenoliths. Data are reported in Tables 3 and 5.

Zircon grains from the monzogranite xenoliths have a weighted mean $^{206}Pb/^{238}U$ age of 122.8 ± 1.8 Ma (Figure 6b), consistent with the ages of the Cretaceous granitic and granodioritic plutons in the Bengbu area, suggesting that the primary magmas were derived from partial melting of NCC basement (~120 Ma; Yang et al. 2010; Liu et al. 2012). Furthermore, the monzogranite xenoliths have high bulk Sr contents (~1200ppm) and Sr/Y ratios (~80) (Table 1), and positive Eu anomalies (Figure 4d), which are identical to the geochemical features of adakitic rocks in the Bengbu area that were interpreted by Liu et al. (2012) to be derived from partial melting of NCC rocks. We infer that the monzogranite xenoliths represent fragments of the Cretaceous plutonic rocks that shortly predate the formation of the lamprophyric dikes.

By contrast, the older Triassic ages (210–230 Ma) of zircons from the banded biotite granitic gneiss xenoliths (Figure 8) overlap ages of metamorphic zircon from the Dabie–Sulu orogenic belt. Such ages have not been reported for NCC rocks. Therefore, it is most likely that these xenoliths did not originate from the NCC crust but rather are related to the South China Block. In addition,

the upper-intercept U–Pb age, although poorly defined, is broadly consistent with protolith ages of the Dabie–Sulu UHP gneiss of the SCB, which resulted from Neoproterozoic magmatism during the breakup of the supercontinent Rodinia along the northern margin of the Yangtze Block (Rowley et al. 1997; Zheng et al. 2003; Huang et al. 2006). Moreover the absence of Jurassic zircon ages (~160 Ma) suggests that these xenoliths did not witness any subsequent metamorphic or melting events. Together, our observations suggest that these xenoliths represent samples of the SCB crust located below the exposed NCC upper crust.

The ca. 1.8 Ga SHRIMP zircon age of the garnet-bearing plagioclase gneiss xenolith is consistent with Palaeoproterozoic granulite facies metamorphism in the southeastern NCC margin (Liu et al. 2009), suggesting that these xenoliths represent NCC basement fragments.

In summary, the xenolith suite represents a surprisingly wide range of crustal rocks of different age and provenance, including fragments of the North China Craton and its younger Cretaceous intrusives as well as 'foreign' fragments that may be related to the South China Craton, which is exposed more than 100 km away from

Table 3. LA-ICP-MS zircon Th/U ratios and isotopic compositions of monzogranite xenoliths from lamprophyre dikes in Jingshan granite.

| Spot	Th/U	Isotopic ratios						Isotopic ages (Ma)		Note
		207Pb*/206Pb*	±%	207Pb*/235 U	±%	206Pb*/206Pb*	±%	206Pb/238 U	±	
0905js-1-1	0.23	0.0539	0.0041	0.0195	0.0004	0.15	0.01	125	3	Rim
0905js-1-2	0.26	0.0532	0.0033	0.0187	0.0004	0.14	0.01	120	2	Rim
0905js-1-3	0.26	0.0485	0.0036	0.0193	0.0004	0.13	0.01	124	2	Rim
0905js-1-4	0.21	0.0621	0.0070	0.0201	0.0004	0.17	0.02	128	3	Rim
0905js-1-5	0.33	0.0505	0.0037	0.0190	0.0003	0.13	0.01	121	2	Rim
0905js-1-6	0.18	0.0507	0.0038	0.0186	0.0004	0.13	0.01	119	2	Rim
0905js-1-7	0.38	0.0535	0.0049	0.0188	0.0004	0.14	0.01	120	3	Rim
0905js-1-8	0.18	0.0491	0.0042	0.0197	0.0004	0.13	0.01	125	3	Rim
0905js-1-9	0.31	0.0481	0.0049	0.0206	0.0004	0.14	0.02	132	3	Rim
0905js-1-10	0.09	0.0666	0.0063	0.0202	0.0005	0.18	0.02	129	3	Rim
0905js-1-11	0.19	0.0635	0.0048	0.0196	0.0005	0.17	0.01	125	3	Rim
0905js-1-12	0.26	0.0503	0.0043	0.0195	0.0005	0.13	0.01	124	3	Rim
0905js-1-13	0.23	0.0467	0.0035	0.0184	0.0003	0.12	0.01	118	2	Rim
0905js-1-14	0.22	0.0491	0.0037	0.0205	0.0004	0.14	0.01	131	3	Rim
0905js-1-15	0.25	0.0494	0.0044	0.0195	0.0004	0.13	0.01	125	2	Rim
0905js-1-16	0.19	0.0519	0.0044	0.0185	0.0004	0.13	0.01	118	3	Rim
0905js-1-17	0.22	0.0547	0.0050	0.0201	0.0005	0.15	0.02	129	3	Rim
0905js-1-18	0.26	0.0494	0.0036	0.0185	0.0003	0.13	0.01	118	2	Rim
0905js-1-19	0.25	0.0490	0.0039	0.0189	0.0004	0.13	0.01	121	2	Rim
0905js-1-20	0.25	0.0486	0.0048	0.0191	0.0004	0.13	0.01	122	3	Rim
0905js-1-21	0.20	0.0473	0.0041	0.0194	0.0005	0.13	0.01	124	3	Rim
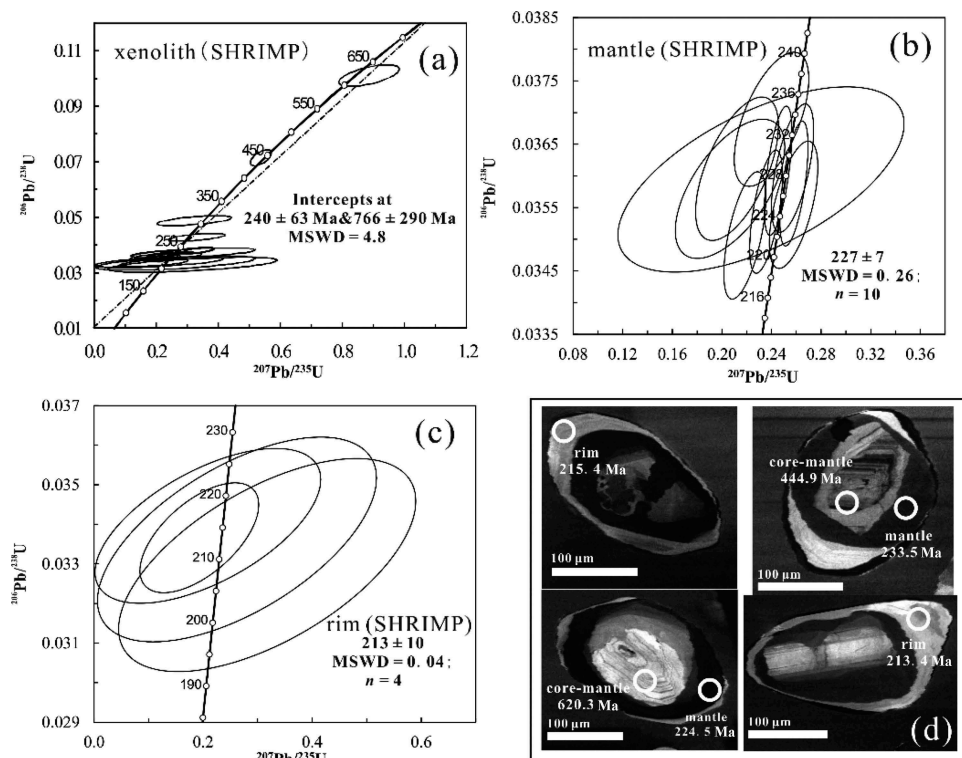
Figure 7. Zircon U–Pb concordia diagrams and CL images for banded biotite granitic gneiss xenoliths within lamprophyre dikes in Jingshan granite. (a) SHRIMP results of banded biotite granitic gneiss xenoliths. (b) Concordant age of the mantle of the zircon. (c) Concordant age of the rim of the zircon. (d) Representative CL images of the dated zircon grains. Data are reported in Table 4.

the emplacement site of the lamprophyres. We will now explore further the geochronological and compositional evidence recorded in the xenoliths and their zircons to test this hypothesis.

5.2. The provenance of the South China crust in the North China cratonic realm

Granitic gneisses constitute one of the major rock types that are exposed widely in the Dabie–Sulu orogen. The highly felsic nature of the banded biotite granitic gneiss xenolith, and the significant enrichment in LILEs, but relative depletion in HFSEs, Sr, and P, are similar to those of Neoproterozoic granites from the Wulian region in the Dabie–Sulu orogen (Huang et al. 2006) and Dabie–Sulu gneisses (see Figure 10a). Therefore, we infer that the banded biotite granitic gneiss xenoliths indeed originated from the SCB upper crust.

SHRIMP U–Pb dating shows that zircons from the banded biotite granitic gneiss xenoliths underwent multiple growth stages. The discordant age and variable Th/U values of core-mantle domains are compatible with a scenario, whereby the zircon grains recrystallized more recently, which variably reset the zircon U–Th–Pb isotope systems (Vavra et al. 1996, 1999; Wu and Zheng 2004; Xia et al. 2009). The mantle growth domains of the same

zircons with concordant ages of 226.7 ± 2.1 Ma show modestly high Th/U ratios (0.01–0.1, Table 4 and Figure 9), and nearly flat patterns from the MREEs to the HREEs $((Yb/Dy)_n < 10$, Table S1 and Figure 9). By contrast, domains with a concordant age of 214.2 ± 4.0 Ma show lower Th/U ratios (<0.01, Table 4) and steeper REE patterns $((Yb/Dy)_n > 10)$.

Hermann et al. (2001) investigated the multi-growth process of zircons accompanying exhumation of the deeply subducted continent crust. They identified typical textural characteristics and REE patterns of zircons formed during UHP metamorphism, followed by lower pressure garnet-granulite-facies conditions with garnets, and amphibolite-facies conditions without garnet. They found that zircons formed under amphibolite-facies conditions in the absence of garnet show very steep REE patterns that are distinct from that of zircon domains formed under HP metamorphic conditions. Accordingly, the steep REE patterns of rim domains of zircons from the banded biotite granitic gneiss xenoliths suggest that they formed in a garnet-free environment, probably during amphibolite-facies retrogression. The mantle domains with flat REE patterns show features of HP metamorphism. However, no UHP indicative mineral inclusions such as diamond, coesite, omphacite, and titan phengite were found after careful petrographic inspection of these zircons. Since previous

Table 4. SHRIMP zircon U–Th elemental and isotopic compositions of banded biotite granitic gneiss xenoliths from lamprophyre dikes in Jingshan granite.

Spot	U (ppm)	Th (ppm)	Th/U	206Pbc%	Pb* (ppm)	Isotopic ratios						Isotopic ages (Ma)		Note
						207Pb*/206Pb*	±%	207Pb*/235 U	±%	206Pb*/238 U	±%	206Pb/238 U	±	
JS-X-2-17.3	265	152	0.57	1.22	16.5	0.0545	3.9	0.54	5.1	0.0715	3.3	444.9	14.2	Core-mantle
JS-X-2-7.2	51.9	52.9	1.02	2.45	4.62	0.0636	8.4	0.89	9.0	0.1010	3.1	620.3	18.6	Core-mantle
JS-X-2-1.1	62.9	27.4	0.44	3.03	2.72	0.0480	30	0.32	30	0.0488	3.0	307.2	9.1	Core-mantle
JS-X-2-4.2	132	54.5	0.41	2.14	4.42	0.0613	15	0.32	15	0.0380	2.6	240.6	6.1	Core-mantle
JS-X-2-5.2	138	21.3	0.15	2.37	5.20	0.0561	22	0.33	22	0.0429	2.6	270.6	7.0	Core-mantle
JS-X-2-9.1	33.7	2.46	0.07	7.48	1.16	0.0621	51	0.32	51	0.0372	4.0	235.6	9.2	Core-mantle
JS-X-2-11.1	140	18.8	0.13	1.30	4.64	0.0641	12	0.34	12	0.0381	2.4	241.2	5.7	Core-mantle
JS-X-2-18.1	232	46.6	0.20	3.08	7.55	0.0356	26	0.18	26	0.0367	2.5	232.0	5.8	Core-mantle
JS-X-2-1.2	308	40.6	0.13	0.67	9.61	0.0516	4.9	0.26	5.4	0.0361	2.3	228.8	5.2	Mantle
JS-X-2-2.1	235	2.74	0.01	0.56	7.22	0.0526	5.8	0.26	6.2	0.0355	2.3	225.1	5.1	Mantle
JS-X-2-6.1	139	9.27	0.07	3.46	4.44	0.0419	17	0.21	17	0.0358	2.5	226.7	5.6	Mantle
JS-X-2-4.1	481	17.4	0.04	0.24	14.9	0.0522	2.8	0.26	3.6	0.0359	2.2	227.2	5.0	Mantle
JS-X-2-7.1	542	23.1	0.04	0.55	16.6	0.0482	4.0	0.24	4.6	0.0354	2.2	224.5	4.9	Mantle
JS-X-2-8.1	491	32.8	0.07	1.13	15.0	0.0452	5.9	0.22	6.3	0.0351	2.3	222.1	5.1	Mantle
JS-X-2-17.2	315	5.49	0.02	1.23	10.1	0.0472	10	0.24	10	0.0369	2.3	233.5	5.4	Mantle
JS-X-2-13.1	345	18.0	0.05	2.08	10.9	0.0426	13	0.21	13	0.0361	2.6	228.7	5.8	Mantle
JS-X-2-14.1	56.2	1.41	0.02	6.63	1.86	0.0467	41	0.23	41	0.0359	3.3	227.6	7.4	Mantle
JS-X-2-15.1	611	45.8	0.07	0.64	19.1	0.0493	2.9	0.25	3.7	0.0361	2.3	228.5	5.2	Mantle
JS-X-2-16.1	17.0	0.02	0.00	11.1	0.54	0.0699	70	0.32	70	0.0330	6.7	209.1	13.7	Rim
JS-X-2-3.1	34.7	0.07	0.00	7.01	1.08	0.0416	46	0.19	46	0.0337	3.4	213.4	7.1	Rim
JS-X-2-10.1	16.6	0.02	0.00	16.6	0.57	0.0566	80	0.26	80	0.0336	6.3	213.1	13.2	Rim
JS-X-2-12.1	26.8	0.31	0.01	9.88	0.87	0.0446	81	0.21	81	0.0340	4.7	215.3	10.0	Rim

Note: Pbc and Pb* indicate the common and radiogenic portions, respectively.

Table 5. SHRIMP zircon U–Th elemental and isotopic compositions of garnet-bearing plagioclase gneiss xenoliths from lamprophyre dikes in Jingshan granite.

Spot	U (ppm)	Th (ppm)	Th/U	206Pbc%	Pb* (ppm)	Isotopic ratios						Isotopic ages (Ma)		Note
						207Pb*/206Pb*	±%	207Pb*/235U	±%	206Pb*/238U	±%	206Pb/238U	±	
JS-X-3-1.1	195	158	0.81	0.05	53.5	0.1100	0.71	4.83	2.4	0.3185	2.24	1782	35	Rim
JS-X-3-1.2	22.9	30.0	1.31	0.67	10.8	0.2138	1.92	16.06	3.2	0.5445	2.62	2802	59	Core-rim
JS-X-3-1.3	1144	738	0.65	0.03	503	0.2073	0.17	14.62	2.3	0.5117	2.27	2664	50	Core
JS-X-3-2.1	148	207	1.40	0.37	42.0	0.1110	0.97	5.04	2.5	0.3296	2.26	1836	36	Rim

Note: Pbc and Pb* indicate the common and radiogenic portions, respectively.
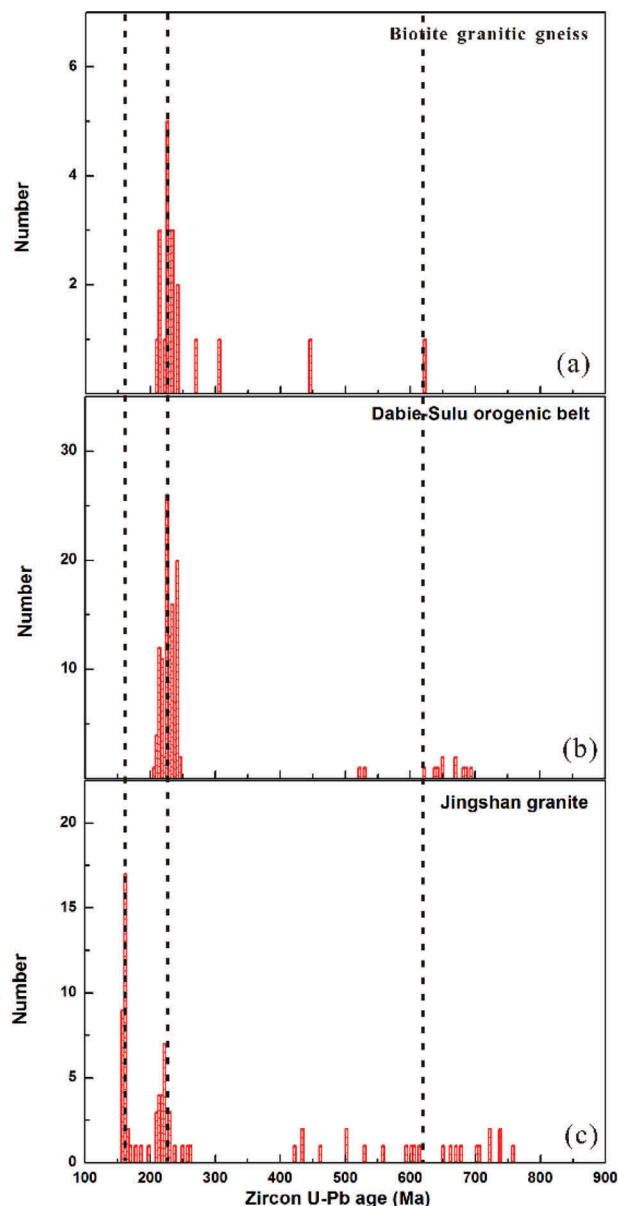
Figure 8. Histograms of U–Pb ages for zircons. (a) Data for zircons from banded biotite granitic gneiss xenoliths. (b) Data for zircons from metamorphic rocks in the Dabie–Sulu orogenic belt (data from Hacker et al. 1998, 2000; Yang et al. 2003; Liu et al. 2004a, 2004b, 2005, 2008; Wan et al. 2005; Zhao et al. 2005, 2006a, 2006b, 2007; Zheng et al. 2005; Liu et al. 2006a, 2006b; Wu et al. 2006). (c) Data for zircons from Jingshan granite (data from Xu et al. 2005 2013).

studies on the Dabie–Sulu terrain show that coesite- and diamond-bearing UHP mineral assemblages commonly occur as inclusions in zircons from the Dabie–Sulu UHPM terrain (e.g. Liu et al. 2004a), the inclusion mineral assemblages found in zircons from the banded biotite granitic gneiss xenoliths likely suggest that they formed during the HP eclogite-facies rather than during
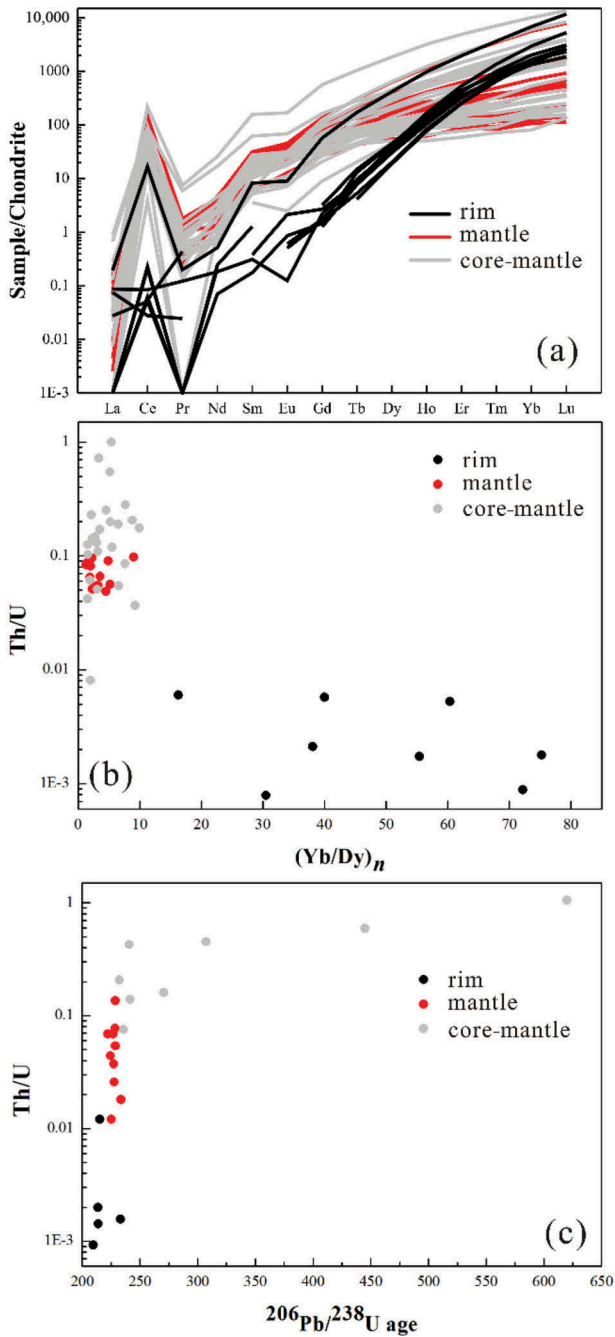
Figure 9. (a) Chondrite-normalized rare earth element (REE) patterns of zircons from biotite granitic gneiss xenoliths. (b) Diagrams for Th/U vs. (Yb/Dy)n of zircons from biotite granitic gneiss xenoliths. Data of zircon LA-ICP-MS trace element contents are reported in Table S1. (c) Diagrams for Th/U vs. ^{206}Pb/^{238}U age of zircons from biotite granitic gneiss xenoliths. Data of zircon SHRIMP Th and U contents are reported in Table 4.

UHP metamorphism. Zheng *et al.* (2009) reviewed zircon U–Pb ages in protolith crystallization and subduction-zone eclogite sub-facies in the Dabie–Sulu orogen. They estimated that the UHP eclogite-facies metamorphism lasted

from 240 to 225 Ma, HP eclogite-facies recrystallization from 225 to 215 Ma, and the amphibolite-facies retrograde event from 215 to 205 Ma. Our results show that the rocks of probable SCB origin that were emplaced into the North China crust experienced HP eclogite-facies metamorphism and an amphibolite-facies retrograde event during the continental collision. However, there is no evidence that the intruded SCB experienced UHP metamorphism.

5.3. A genetic relationship between biotite granitic gneiss xenoliths and Jingshan granite

Previous studies correlated the source rocks of the Jingshan granite with the SCB crust (Guo and Li 2009a; Yang *et al.* 2010; Wang *et al.* 2011; Li *et al.* 2013; Xu *et al.* 2013). A comparison of ages between zircons from the banded biotite granitic gneiss xenoliths and those from the Jingshan granite (Figure 8) reveals the same age distribution except for the lack of the 160 Ma event. Therefore, we suggest that these xenoliths from the SCB have a genetic relationship with the Jingshan granites.

Detailed geochemical investigations show that the protoliths of Jingshan granites were derived from orthogneisses with metaluminous features (Guo and Li 2009a; Li *et al.* 2013). Mineralogy and geochemistry of biotite granitic gneiss xenoliths indicate that they may belong to the same orthogneiss and thus resemble source rocks of the Jingshan granites. Recently, Xu *et al.* (2013) carried out a detailed study on the mafic biotite- and garnet-rich enclaves, granites, and aplites from the Jingshan granite and the origin of distinct types of garnets in the Jingshan pluton. They concluded that the majority of the garnets in the mafic enclaves and the granite are of peritectic origin, formed during biotite-dehydration melting. Gardien *et al.* (2000) conducted melting experiments on biotite + plagioclase + quartz gneisses at 10, 15, and 20 kbar between 800 and 900°C. The banded biotite granitic gneiss xenoliths are similar to the starting materials of their experiments, and the results show that the mineral assemblages derived from the molten products are indeed similar to those in the Jingshan granite. Therefore, we suggest that the banded biotite granitic gneiss xenoliths represent the protolith lithology of the Jingshan granite.

Trace element features of the banded granitic gneiss xenoliths and the Jingshan granites (data from Li *et al.* 2013; Xu *et al.* 2013) show a marked difference (Figure 10) and we will test whether these differences are in accordance with the proposed genetic relationship: the Jingshan granite shows distinctively lower Th, P, and HFSEs (Nb, Ta, Zr, Hf, and Ti) as compared to the xenoliths. The Jingshan granites also have low LREEs, which are significantly different from those of the xenoliths. Such low Th and LREEs in the granites may be related to residual epidote or allanite. As shown in Figure 11, with the banded granitic gneiss xenoliths as
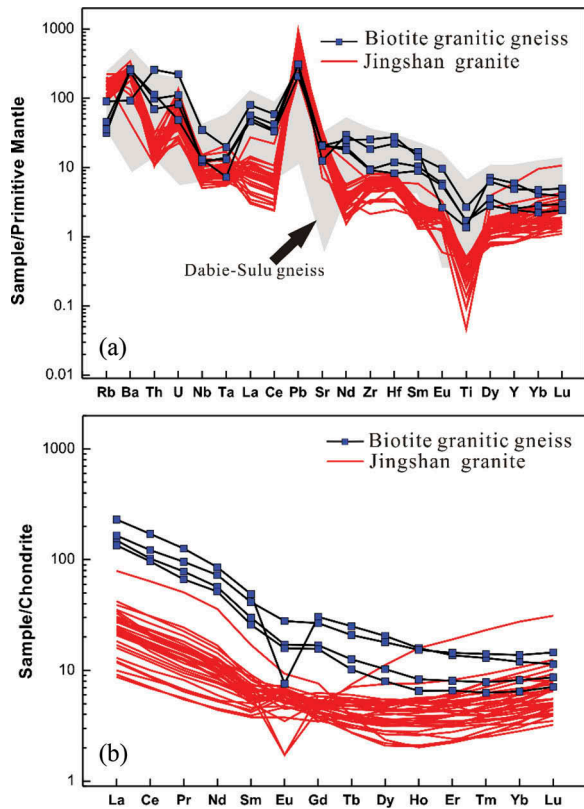
Figure 10. Comparison of the trace element (a) and rare earth element (REE) (b) data of banded biotite granitic gneiss xenoliths with those of the Jingshan granite and Dabie–Sulu gneisses. The data of Jingshan granite are from Li *et al.* (2013) and Xu *et al.* (2013). The data of Dabie–Sulu gneisses are from Li *et al.* (2000), Bryant *et al.* (2004), Zhao *et al.* (2007a, 2007b), Tang *et al.* (2008) and Xia *et al.* (2010). Compositions of chondrite and primitive mantle are from Sun and McDonough (1989).
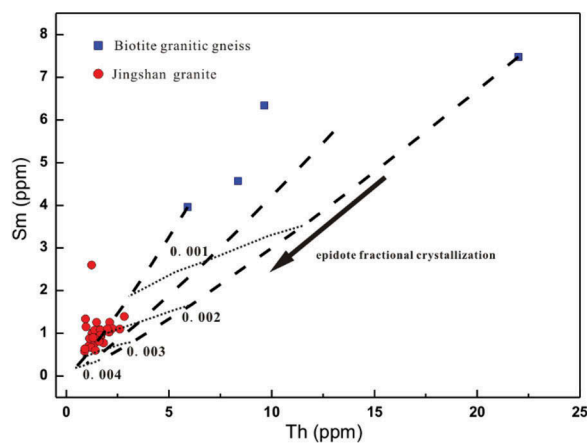

Figure 11. Sm vs. Th of banded biotite granitic gneiss xenoliths and Jingshan granite. Fractional crystallization of epidote minerals is modelled, with the banded biotite granitic gneiss xenolith as the starting material (dashed lines). The partition coefficient of Th is 648 from Ewart and Griffin (1994), and the partition coefficient of Sm is 756 from Mahood and Hildreth (1983).

the protoliths, only a small amount of residual epidote minerals remaining in the residual magma (0.2–0.3%) is sufficient to explain the low LREE and Th features of Jingshan granite. Epidote and allanite have been reported to be obtained from the biotite- and garnet-rich melt residues in the Jingshan pluton (Li *et al.* 2013; Xu *et al.* 2013), supporting this interpretation. However, the P and the negative HFSE anomaly cannot be explained by the role of accessory minerals such as titanite, rutile, or apatite since the proportion of these minerals in the rocks is too low to influence the whole-rock geochemical patterns.

5.4. Implications for the early Mesozoic tectonic evolution of the eastern NCC

The Jurassic granites in the southeastern part of the NCC suggest the presence of the subduction-related thickened continental crust along the southern margin of the Craton (Guo and Li 2009a; Yang *et al.* 2010; Jiang *et al.* 2012, Li *et al.* 2013). However, the mechanism of how the deeply buried SCB continental crust was emplaced within or below the southern margin of the NCC remains unclear (see Yang *et al.* 2010; Li *et al.* 2013). Our finding indicates that the material emplaced into the NCC mainly consists of granitic gneiss from the South China plate (Figure 12b), which experienced deep burial and exhumation during continental collision around 240–225 million years ago, but probably without experiencing UHP metamorphism, which is recorded at the same time for the SCB rocks within the Dabie–Sulu regions (Figure 12a). However, an age of 210 Ma, as recorded for the youngest zircons from the banded biotite granitic gneiss xenoliths, suggests that the SCB rocks suffered later metamorphism. This metamorphism was followed by melt generation ~50 million years later, as recorded by the age of zircons from the Jingshan granite. All models that try to decipher the tectonic evolution and origin of Jingshan granite must consider the above observation.

Yang *et al.* (2010) suggested that the SCB was emplaced below the NCC lithosphere along the Tan-Lu fault zone in Triassic times (245–220 Ma) during continental collision. The Late Jurassic plutons such as the Jingshan granites formed by the upwelling of the asthenosphere after the slab break-off and delamination of the thickened NCC lithosphere. However, our research shows that the SCB was emplaced directly below or possibly even within the NCC crust, rather than at mantle depths below the NCC lithosphere. Our data and their interpretation are thus in contrast to previous models. Their model also encounters some difficulties as pointed out by Li *et al.* (2013).

Li *et al.* (2013) proposed a crustal flow model to explain the origin of the Bengbu Jurassic granite. They suggest that the soft and partially molten felsic crust of the
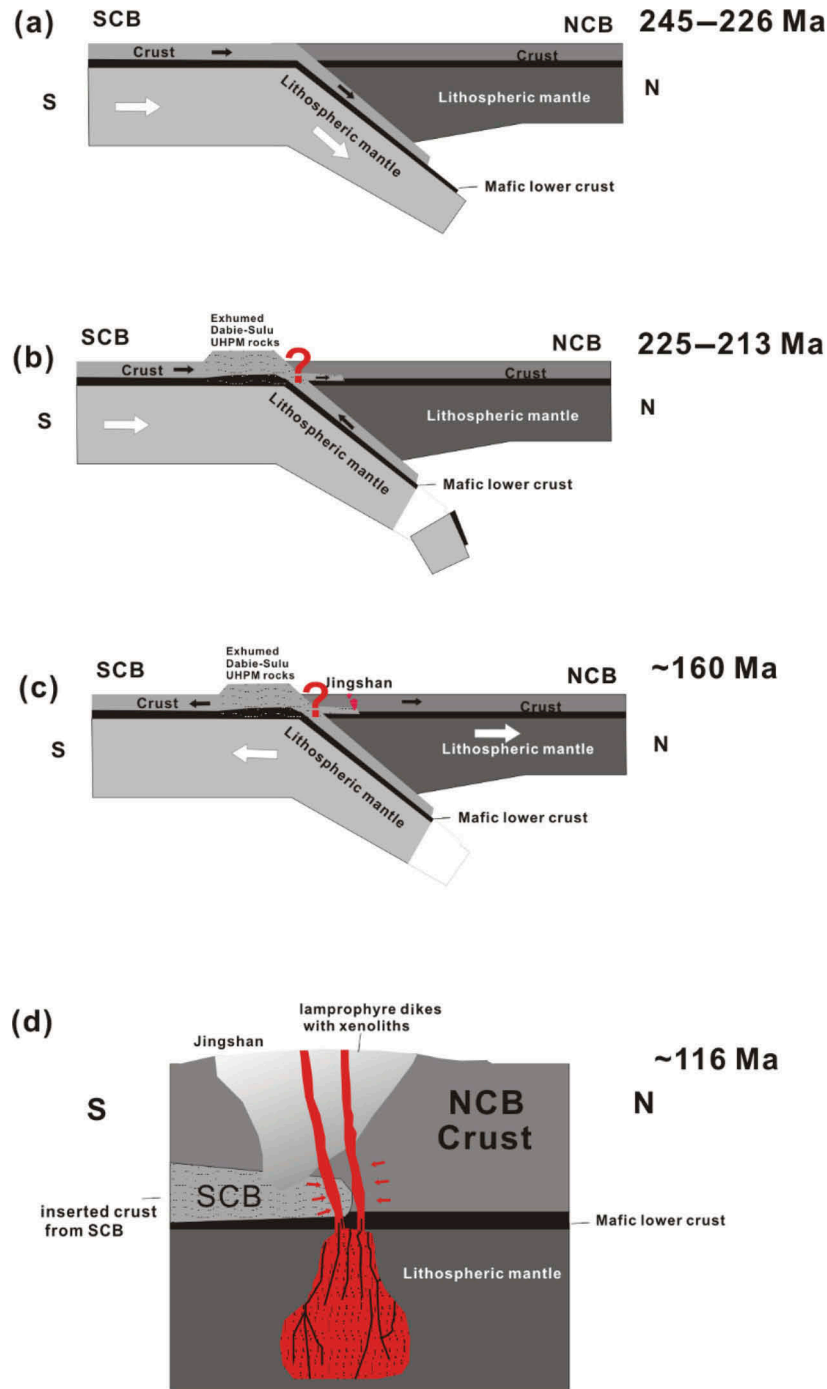
Figure 12. Our proposed model of Mesozoic tectonic setting of the southeastern margin of the NCC. (a) Cartoons showing continental subduction and UHPM rock exhumation processes during collision between the SCB and NCC in the Early and Middle Triassic. (b) Cartoons showing UHPM rock exhumation processes after breaking off of the slab and the intrusion of the felsic crust of the South China plate into the North China crust in the Middle and Late Triassic. (c) Cartoon showing the melting of the South China crust and formation of Jingshan pluton in the Jurassic. (d) Cartoon showing the intruding of mantle-derived lamprophyre dikes into Jingshan granite at 116 Ma, taking along different types of crustal xenoliths through its ascending channel. Abbreviations: SCB, South China Block; NCC, North China Block; UHPM, UHP metamorphism.

SCB was injected into the NCC crust in Late Jurassic times. Partial crustal melts then ascended to form granites. This model could explain most observations in the Bengbu

area. However, the emplacement time of the SCB crust is constrained as Late Triassic (210 Ma) based on our present study. In addition, the study of Jurassic granitic plutons

from the Jiaobei terrain located at the NCC southeastern margin close to the Sulu orogen indicates that these also originated from partial melting of the SCB-type crust (Jiang *et al.* 2012), which is hard to account for by the crustal flow model.

We therefore propose an alternative model: following deep burial of the SCB continental crust during collision, a high-density mafic crust broke away by delamination, exhuming the deeply subducted crust driven by the buoyancy of the remaining, more felsic continental crust (Ernst *et al.* 1997; Zheng *et al.* 2009) (Figure 12a). While the SCB and the NCC remained under compression due to plate convergence (Wang and Lin 2002; Liu *et al.* 2003), part of the exhumed upper crust never experienced deep subduction under UHP conditions and was underthrust beneath the root of the orogen at an intermediate crustal level. The felsic crust of the SCB was thus emplaced below and into the NCC through continued compression (Figure 12b). Recent experimental work on the rheology of mafic granulites suggests that in the presence of moderate amounts of water (~0.05–0.08 wt% H_2O), the mafic crust is likely to be a weak layer in the lithosphere (Wang *et al.* 2012). Many investigations have shown that the North China granulitic continental lower crust preserves a significant amount of structurally bound water in nominally anhydrous minerals (e.g. Xia *et al.* 2006; Yang *et al.* 2008b). Thus, such a weakened lower crust at the southeastern NCC margin may have allowed the felsic SCB crust to have been emplaced for more than 100 kilometres into or below the NCC (Figure 12b). The felsic SCB melted at ca. 160 Ma and formed the Jingshan granite (Figure 12c), which might have been caused by Jurassic lithospheric extension (Wang and Lin 2002) or radioactive heat production (Clark *et al.* 2011).

Since the discovery of coesite and diamond in the rocks from continental collision belts (e.g. Chopin 1984; Smith 1984; Sobolev and Shatsky 1990; Xu *et al.* 1992), it is established that a low density continental crust can be subducted to mantle depth and then rapidly exhumed (Zheng *et al.* 2003). Since the timing and physical process of crustal exhumation are not fully understood, our proposed model for the superposition of SCB and NCC crustal rocks is somewhat speculative. However, our study reveals that part of the subducted SCB crust might be interleaved with the crust of the overlying NCC. Detailed structural and geophysical data of the NCC southeastern margin are needed to test this model in future studies.

6. Conclusions

Crustal xenoliths from the lamprophyre dikes in the Jingshan granite provide an opportunity to understand the composition and formation of deep crusts in the NCC southeastern margin. We arrive at the following conclusions based on whole-rock geochemistry and zircon chronology combined with zircon trace element data.

Zircon U–Pb dating and compositional data show that the different types of xenoliths have different origins.

(1) Monzogranite xenoliths are locally derived and share compositional and age similarities with the Bengu uplift Late Jurassic to Upper Cretaceous intrusive suite.

(2) Major- and trace-element content and zircon ages from the banded biotite granitic gneiss xenoliths suggest that they originated from the SCB, which provides the first direct evidence that such a crust was emplaced below or within the NCC southeastern margin.

(3) Zircon chronology and lack of typical coesite or diamond inclusions show that unlike UHP rocks of the SCB exposed today in the Dabie–Sulu metamorphic belt, the SCB rocks that were emplaced in the NNC realm never experienced UHP conditions and were even partially exhumed before being emplaced into or below the NCC crust.

(4) The garnet gneisses gave much older zircon ages (1.8 Ga) and therefore likely represent the 'local' North China Craton lithologies into which the SCB rocks were tectonically emplaced.

(5) Subsequent melting of SCB lithologies generated the Jingshan granite during uplift and extension during Late Jurassic and Early Cretaceous times.

(6) Lamprophyric dikes that carried the xenoliths from various levels of the crust represent the latest magmatic event at 116 Ma, shortly following the youngest granites in the area and probably reflect melting of the mantle lithosphere below the Bengu uplift.

References

Andersen, T., 2002, Correction of common lead in U–Pb analyses that do not report [204]Pb: Chemical Geology, v. 192, p. 59–79. doi:10.1016/S0009-2541(02)00195-X.

Black, L.P., Kamo, S.L., Allen, C.M., Aleinikoff, J.N., Davis, D.W., Korsch, R.J., and Foudoulis, C., 2003, TEMORA 1: A new zircon standard for Phanerozoic U–Pb geochronology: Chemical Geology, v. 200, p. 155–170. doi:10.1016/S0009-2541(03)00165-7.

Bryant, D.L., Ayers, J.C., Gao, S., Miller, C.F., and Zhang, H., 2004, Geochemical, age, and isotopic constraints on the location of the Sino–Korean/Yangtze Suture and evolution of the Northern Dabie Complex, east central China: Geological Society of America Bulletin, v. 116, p. 698–717. doi:10.1130/B25302.2.

Chopin, C., 1984, Coesite and pure pyrope in high-grade blueschists of the Western Alps: A first record and some consequences: Contributions to Mineralogy and Petrology, v. 86, p. 107–118. doi:10.1007/BF00381838.

Clark, C., Fitzsimons, I.C., Healy, D., and Harley, S.L., 2011, How does the continental crust get really hot? Elements, v. 7, p. 235–240.

Ernst, W., Maruyama, S., and Wallis, S., 1997, Buoyancy-driven, rapid exhumation of ultrahigh-pressure metamorphosed continental crust: Proceedings of the National Academy of Sciences, v. 94, p. 9532–9537. doi:10.1073/pnas.94.18.9532.

Ewart, A., and Griffin, W., 1994, Application of proton-microprobe data to trace-element partitioning in volcanic rocks: Chemical Geology, v. 117, p. 251–284. doi:10.1016/0009-2541(94)90131-7.

Frei, D., Liebscher, A., Franz, G., and Dulski, P., 2004, Trace element geochemistry of epidote minerals: Reviews in Mineralogy and Geochemistry, v. 56, p. 553–605. doi:10.2138/gsrmg.56.1.553.

Gao, Y., Hou, Z., Kamber, B.S., Wei, R., Meng, X., and Zhao, R., 2007, Lamproitic rocks from a continental collision zone: Evidence for recycling of subducted tethyan oceanic sediments in the mantle beneath southern Tibet: Journal of Petrology, v. 48, p. 729–752. doi:10.1093/petrology/egl080.

Gardien, V., Thompson, A.B., and Ulmer, P., 2000, Melting of biotite plus plagioclase plus quartz gneisses: The role of H_2O in the stability of amphibole: Journal of Petrology, v. 41, p. 651–666. doi:10.1093/petrology/41.5.651.

Gu, H.-O., Xiao, Y., Santosh, M., Li, W.-Y., Yang, X., Pack, A., and Hou, Z., 2013, Spatial and temporal distribution of Mesozoic adakitic rocks along the Tan-Lu fault, Eastern China: Constraints on the initiation of lithospheric thinning: Lithos, v. 177, p. 352–365. doi:10.1016/j.lithos.2013.07.011.

Guo, F., Fan, W., Wang, Y., and Zhang, M., 2004, Origin of early Cretaceous calc-alkaline lamprophyres from the Sulu orogen in eastern China: Implications for enrichment processes beneath continental collisional belt: Lithos, v. 78, p. 291–305. doi:10.1016/j.lithos.2004.05.001.

Guo, S., and Li, S., 2009a, Petrochemical characteristics of leucogranite and a case study of Bengbu leucogranites: Chinese Science Bulletin, v. 54, p. 1923–1930. doi:10.1007/s11434-009-0355-4.

Guo, S., and Li, S., 2009b, SHRIMP zircon U-Pb ages for the Paleoproterozoic metamorphic-magmatic events in the southeast margin of the North China Craton: Science in China Series D-Earth Sciences, v. 52, p. 1039–1045. doi:10.1007/s11430-009-0099-7.

Hacker, B.R., Ratschbacher, L., Webb, L., Ireland, T., Walker, D., and Shuwen, D., 1998, U/Pb zircon ages constrain the architecture of the ultrahigh-pressure Qinling–Dabie Orogen,

China: Earth and Planetary Science Letters, v. 161, p. 215–230. doi:10.1016/S0012-821X(98)00152-6.

Hacker, B.R., Ratschbacher, L., Webb, L., McWilliams, M.O., Ireland, T., Calvert, A., Dong, S., Wenk, H.-R., and Chateigner, D., 2000, Exhumation of ultrahigh-pressure continental crust in east central China: Late Triassic-Early Jurassic tectonic unroofing: Journal of Geophysical Research, v. 105, p. 13339–13364. doi:10.1029/2000JB900039.

Hermann, J., Rubatto, D., Korsakov, A., and Shatsky, V.S., 2001, Multiple zircon growth during fast exhumation of diamondiferous, deeply subducted continental crust (Kokchetav Massif, Kazakhstan): Contributions to Mineralogy and Petrology, v. 141, p. 66–82. doi:10.1007/s004100000218.

Hou, Z., and Wang, C., 2007, Determination of 35 trace elements in geological samples by inductively coupled plasma mass spectrometry: Journal of University of Science and Technology of China, v. 37, p. 940–944.

Huang, J., Zheng, Y.-F., Zhao, Z.-F., Wu, Y.-B., Zhou, J.-B., and Liu, X., 2006, Melting of subducted continent: Element and isotopic evidence for a genetic relationship between Neoproterozoic and Mesozoic granitoids in the Sulu orogen: Chemical Geology, v. 229, p. 227–256. doi:10.1016/j.chemgeo.2005.11.007.

Iizuka, T., and Hirata, T., 2004, Simultaneous determinations of U-Pb age and REE abundances for zircons using ArF excimer laser ablation-ICPMS: Geochemical Journal-Japan-, v. 38, p. 229–242. doi:10.2343/geochemj.38.229.

Ireland, T., Calvert, A., Dong, S., Wenk, H.-R., and Chateigner, D., 2000, Exhumation of ultrahigh-pressure continental crust in east central China: Late Triassic-Early Jurassic tectonic unroofing: Journal of Geophysical Research, v. 105, p. 13339–13364. doi:10.1029/2000JB900039.

Jahn, B.-M., Cornichet, J., Cong, B., and Yui, T.-F., 1996, Ultrahigh-εNd eclogites from an ultrahigh-pressure metamorphic terrane of China: Chemical Geology, v. 127, p. 61–79. doi:10.1016/0009-2541(95)00108-5.

Jamieson, R.A., Unsworth, M.J., Harris, N.B.W., Rosenberg, C.L., and Schulmann, K., 2011, Crustal melting and the flow of mountains: Elements, v. 7, p. 253–260. doi:10.2113/gselements.7.4.253.

Jiang, N., Chen, J., Guo, J., and Chang, G., 2012, In situ zircon U–Pb, oxygen and hafnium isotopic compositions of Jurassic granites from the North China craton: Evidence for Triassic subduction of continental crust and subsequent metamorphism-related 18O depletion: Lithos, v. 142–143, p. 84–94. doi:10.1016/j.lithos.2012.02.018.

Le Bas, M., Le Maitre, R., Streckeisen, A., and Zanettin, B., 1986, A chemical classification of volcanic rocks based on the total alkali-silica diagram: Journal of Petrology, v. 27, p. 745–750. doi:10.1093/petrology/27.3.745.

Li, S., Wang, S.-J., Guo, S., Xiao, Y., Liu, Y., Liu, S.-A., He, Y., and Liu, J., 2013, Geochronology and geochemistry of leucogranites from the southeast margin of the North China block: Origin and migration: Gondwana Research, In press. doi:10.1016/j.gr.2012.06.009.

Li, S., Xiao, Y., Liou, D., Chen, Y., Ge, N., Zhang, Z., Sun, -S.-S., Cong, B., Zhang, R., and Hart, S.R., 1993, Collision of the North China and Yangtse Blocks and formation of coesite-bearing eclogites: Timing and processes: Chemical Geology, v. 109, p. 89–111. doi:10.1016/0009-2541(93)90063-O.

Li, S.G., Jagoutz, E., Chen, Y.Z., and Li, Q.L., 2000, Sm-Nd and Rb-Sr isotopic chronology and cooling history of ultrahigh pressure metamorphic rocks and their country rocks at

Shuanghe in the Dabie Mountains, Central China: Geochimica Et Cosmochimica Acta, v. 64, p. 1077–1093. doi:10.1016/S0016-7037(99)00319-1.

Liu, F., Gerdes, A., Liou, J., Xue, H., and Liang, F., 2006a, SHRIMP U-Pb zircon dating from Sulu-Dabie dolomitic marble, eastern China: Constraints on prograde, ultrahigh-pressure and retrograde metamorphic ages: Journal of Metamorphic Geology, v. 24, p. 569–589. doi:10.1111/j.1525-1314.2006.00655.x.

Liu, F., Gerdes, A., Zeng, L., and Xue, H., 2008, SHRIMP U–Pb dating, trace elements and the Lu–Hf isotope system of coesite-bearing zircon from amphibolite in the SW Sulu UHP terrane, eastern China: Geochimica Et Cosmochimica Acta, v. 72, p. 2973–3000. doi:10.1016/j.gca.2008.04.007.

Liu, F., Liou, J.G., and Xu, Z., 2005, U-Pb SHRIMP ages recorded in the coesite-bearing zircon domains of para-gneisses in the southwestern Sulu terrane, eastern China: New interpretation: American Mineralogist, v. 90, p. 790–800. doi:10.2138/am.2005.1677.

Liu, F., Xu, Z., Liou, J., and Song, B., 2004a, SHRIMP U–Pb ages of ultrahigh-pressure and retrograde metamorphism of gneisses, south-western Sulu terrane, eastern China: Journal of Metamorphic Geology, v. 22, p. 315–326. doi:10.1111/j.1525-1314.2004.00516.x.

Liu, F., Xu, Z., and Xue, H., 2004b, Tracing the protolith, UHP metamorphism, and exhumation ages of orthogneiss from the SW Sulu terrane (eastern China): SHRIMP U–Pb dating of mineral inclusion-bearing zircons: Lithos, v. 78, p. 411–429. doi:10.1016/j.lithos.2004.08.001.

Liu, F.L., Xu, Z.Q., Xie, H.M., and Zhao, K.Z., 2006b, Ultrahigh-pressure and retrograde metamorphic ages for paleozoic protolith of paragneiss in the main drill hole of the Chinese Continental Scientific Drilling Project (CCSD-MH), SW Sulu UHP Terrane: Acta Geologica Sinica-English Edition, v. 80, p. 336–348.

Liu, S., Heller, P.L., and Zhang, G., 2003, Mesozoic basin development and tectonic evolution of the Dabieshan oro-genic belt, central China: Tectonics, v. 22, p. 1038. doi:10.1029/2002TC001390.

Liu, S.-A., Li, S., Guo, S., Hou, Z., and He, Y., 2012, The Cretaceous adakitic–basaltic–granitic magma sequence on south-eastern margin of the North China Craton: Implications for lithospheric thinning mechanism: Lithos, v. 134–135, p. 163–178. doi:10.1016/j.lithos.2011.12.015.

Liu, Y.-C., Wang, A.-D., Rolfo, F., Groppo, C., Gu, X.-F., and Song, B., 2009, Geochronological and petrological con-straints on Palaeoproterozoic granulite facies metamorphism in southeastern margin of the North China Craton: Journal of Metamorphic Geology, v. 27, p. 125–138. doi:10.1111/j.1525-1314.2008.00810.x.

Ludwig, K.R., 2001, Users manual for Isoplot/Ex (rev. 2.49): A geochronological toolkit for Microsoft Excel: Berkley.

Mahood, G., and Hildreth, W., 1983, Large partition coefficients for trace elements in high-silica rhyolites: Geochimica Et Cosmochimica Acta, v. 47, p. 11–30. doi:10.1016/0016-7037(83)90087-X.

Pearce, N.J., Perkins, W.T., Westgate, J.A., Gorton, M.P., Jackson, S.E., Neal, C.R., and Chenery, S.P., 1997, A com-pilation of new and published major and trace element data for NIST SRM 610 and NIST SRM 612 glass reference materials: Geostandards Newsletter, v. 21, p. 115–144. doi:10.1111/j.1751-908X.1997.tb00538.x.

Rock, N.M.S., 1987, The nature and origin of lamprophyres: An overview: Geological Society, London, Special Publications, v. 30, p. 191–226. doi:10.1144/GSL.SP.1987.030.01.09.

Rowley, D., Xue, F., Tucker, R., Peng, Z., Baker, J., and Davis, A., 1997, Ages of ultrahigh pressure metamorphism and protolith orthogneisses from the eastern Dabie Shan: U/Pb zircon geochronology: Earth and Planetary Science Letters, v. 151, p. 191–203. doi:10.1016/S0012-821X(97)81848-1.

Rudnick, R., and Gao, S., 2003, Composition of the continental crust: Treatise on Geochemistry, v. 3, p. 1–64. doi:10.1016/B0-08-043751-6/03016-4.

Shutong, X., Okay, A., Shouyuan, J., Sengor, A., Wen, S., Yican, L., and Laili, J., 1992, Diamond from the Dabie Shan meta-morphic rocks and its implication for tectonic setting: Science, v. 256, p. 80–82. doi:10.1126/science.256.5053.80.

Smith, D.C., 1984, Coesite in clinopyroxene in the Caledonides and its implications for geodynamics: Nature, v. 310, p. 641–644. doi:10.1038/310641a0.

Smith, M.E., Singer, B.S., Carroll, A.R., and Fournelle, J.H., 2008, Precise dating of biotite in distal volcanic ash: Isolating subtle alteration using 40Ar/39Ar laser incremental heating and electron microprobe techniques: American Mineralogist, v. 93, p. 784–795. doi:10.2138/am.2008.2517.

Sobolev, N., and Shatsky, V., 1990, Diamond inclusions in gar-nets from metamorphic rocks: A new environment for dia-mond formation: Nature, v. 343, p. 742–746. doi:10.1038/343742a0.

Stevens, G., Villaros, A., and Moyen, J.-F., 2007, Selective peritectic garnet entrainment as the origin of geochemical diversity in S-type granites: Geology, v. 35, p. 9. doi:10.1130/G22959A.1.

Sun, -S.-S., and McDonough, W., 1989, Chemical and isotopic systematics of oceanic basalts: Implications for mantle com-position and processes: Geological Society, London, Special Publications, v. 42, p. 313–345. doi:10.1144/GSL.SP.1989.042.01.19.

Tang, J., Zheng, Y.-F., Wu, Y.-B., Gong, B., Zha, X., and Liu, X., 2008, Zircon U–Pb age and geochemical constraints on the tectonic affinity of the Jiaodong terrane in the Sulu orogen, China: Precambrian Research, v. 161, p. 389–418. doi:10.1016/j.precamres.2007.09.008.

Vavra, G., Gebauer, D., Schmid, R., and Compston, W., 1996, Multiple zircon growth and recrystallization during poly-phase late carboniferous to Triassic metamorphism in gran-ulites of the Ivrea Zone (Southern Alps): An ion microprobe (SHRIMP) study: Contributions to Mineralogy and Petrology, v. 122, p. 337–358. doi:10.1007/s004100050132.

Vavra, G., Schmid, R., and Gebauer, D., 1999, Internal morphol-ogy, habit and U-Th-Pb microanalysis of amphibolite-to-granulite facies zircons: Geochronology of the Ivrea Zone (Southern Alps): Contributions to Mineralogy and Petrology, v. 134, p. 380–404. doi:10.1007/s004100050492.

Wan, Y., Li, R., Wilde, S.A., Liu, D., Chen, Z., Yan, L., Song, T., and Yin, X., 2005, UHP metamorphism and exhumation of the Dabie Orogen, China: Evidence from SHRIMP dating of zircon and monazite from a UHP granitic gneiss cobble from the Hefei Basin: Geochimica Et Cosmochimica Acta, v. 69, p. 4333–4348. doi:10.1016/j.gca.2005.03.055.

Wang, Q.-C., and Lin, W., 2002, Geodynamics of the Dabieshan collisional orogenic belt: Earth Science Frontiers, v. 9, p. 257–266.

Wang, S.-J., Li, S.-G., and Liu, S.-A., 2013, The origin and evolution of low-δ18O magma recorded by multi-growth zircons in granite: Earth and Planetary Science Letters, v. 373, p. 233–241. doi:10.1016/j.epsl.2013.05.009.

Wang, X., Chen, J., Griffin, W.L., O'Reilly, S.Y., Huang, P.Y., and Li, X., 2011, Two stages of zircon crystallization in the Jingshan monzogranite, Bengbu Uplift: Implications for the

syn-collisional granites of the Dabie–Sulu UHP orogenic belt and the climax of movement on the Tan-Lu fault: Lithos, v. 122, p. 201–213. doi:10.1016/j.lithos.2010.12.014.

Wang, Y.F., Zhang, J.F., Jin, Z.M., and Green Ii, H.W., 2012, Mafic granulite rheology: Implications for a weak continental lower crust: Earth and Planetary Science Letters, v. 353–354, p. 99–107. doi:10.1016/j.epsl.2012.08.004.

Wiedenbeck, M., Alle, P., Corfu, F., Griffin, W., Meier, M., Oberli, F., Quadt, A.V., Roddick, J., and Spiegel, W., 1995, Three natural zircon standards for U-Th-Pb, Lu-Hf, trace element and REE analyses: Geostandards Newsletter, v. 19, p. 1–23. doi:10.1111/j.1751-908X.1995.tb00147.x.

Williams, I.S., 1998, U–Th–Pb geochronology by ion microprobe, in McKibben, M.A., Shanks III, W.C., and Ridley, W. I., Eds., Applications of Microanalytical Techniques to Understanding Mineralizing Processes, Reviews in Economic Geology, volume Vol. 7, p. 1–35.

Wu, Y., and Zheng, Y., 2004, Genesis of zircon and its constraints on interpretation of U-Pb age: Chinese Science Bulletin, v. 49, p. 1554–1569. doi:10.1007/BF03184122.

Wu, Y.-B., Zheng, Y.-F., Zhao, Z.-F., Gong, B., Liu, X., and Wu, F.-Y., 2006, U–Pb, Hf and O isotope evidence for two episodes of fluid-assisted zircon growth in marble-hosted eclogites from the Dabie orogen: Geochimica Et Cosmochimica Acta, v. 70, p. 3743–3761. doi:10.1016/j.gca.2006.05.011.

Xia, Q.-K., Yang, X.-Z., Deloule, E., Sheng, Y.-M., and Hao, Y.-T., 2006, Water in the lower crustal granulite xenoliths from Nushan, eastern China: Journal of Geophysical Research, v. 111, p. B11202. doi:10.1029/2006JB004296.

Xia, Q.-X., Zheng, Y.-F., and Hu, Z., 2010, Trace elements in zircon and coexisting minerals from low-T/UHP metagranite in the Dabie orogen: Implications for action of supercritical fluid during continental subduction-zone metamorphism: Lithos, v. 114, p. 385–412. doi:10.1016/j.lithos.2009.09.013.

Xia, Q.-X., Zheng, Y.-F., Yuan, H., and Wu, F.-Y., 2009, Contrasting Lu–Hf and U–Th–Pb isotope systematics between metamorphic growth and recrystallization of zircon from eclogite-facies metagranites in the Dabie orogen, China: Lithos, v. 112, p. 477–496. doi:10.1016/j.lithos.2009.04.015.

Xu, L., Xiao, Y., Wu, F., Li, S., Simon, K., and Wörner, G., 2013, Anatomy of garnets in a Jurassic granite from the south-eastern margin of the North China Craton: Magma sources and tectonic implications: Journal of Asian Earth Sciences, v. 78, p. 198–221. doi:10.1016/j.jseaes.2012.11.026.

Xu, S.-T., Okay, A.I., Ji, S.-Y., Sengor, A.M.C., Su, W., Liu, Y.-C., and Jiang, L.-L., 1992, Diamond from the Dabie Shan metamorphic rocks and its implication for tectonic setting: Science, v. 256, p. 80–82.

Xu, W., Wang, Q., Yang, D., Liu, X., and Guo, J., 2005, SHRIMP zircon U-Pb dating in Jingshan "migmatitic granite", Bengbu and its geological significance: Science in China Series D: Earth Sciences, v. 48, p. 185–191.

Xu, W.-L., Yang, D.-B., Pei, F.-P., Yang, C.-H., Liu, X.-M., and Hu, Z.-C., 2006, Age of the Wuhe complex in the Bengbu uplift: Evidence from LA-ICP-MS zircon U-Pb dating [J]: Geology in China, v. 1, p. 013.

Yang, D.-B., Xu, W.-L., Wang, Q.-H., and Pei, F.-P., 2010, Chronology and geochemistry of Mesozoic granitoids in the Bengbu area, central China: Constraints on the tectonic evolution of the eastern North China Craton: Lithos, v. 114, p. 200–216. doi:10.1016/j.lithos.2009.08.009.

Yang, J., Wooden, J., Wu, C., Liu, F., Xu, Z., Shi, R., Katayama, I., Liou, J., and Maruyama, S., 2003, SHRIMP U–Pb dating of coesite-bearing zircon from the ultrahigh-pressure metamorphic rocks, Sulu terrane, east China: Journal of Metamorphic Geology, v. 21, p. 551–560. doi:10.1046/j.1525-1314.2003.00463.x.

Yang, J.-H., Wu, F.-Y., Wilde, S.A., Belousova, E., and Griffin, W.L., 2008a, Mesozoic decratonization of the North China block: Geology, v. 36, p. 467–470. doi:10.1130/G24518A.1.

Yang, X.-Z., Deloule, E., Xia, Q.-K., Fan, Q.-C., and Feng, M., 2008b, Water contrast between Precambrian and Phanerozoic continental lower crust in eastern China: Journal of Geophysical Research, v. 113, p. B08207.

Zhao, R., Liou, J.G., Zhang, R.Y., and Li, T., 2006a, SHRIMP U-Pb zircon dating of the Rongcheng eclogite and associated peridotite: New constraints for ultrahigh-pressure metamorphism of mantle-derived mafic-ultramafic bodies from the Sulu terrane: Special Papers-Geological Society Of America, v. 403, p. 115.

Zhao, R., Liou, J.G., Zhang, R.Y., and Wooden, J.L., 2005, SHRIMP U-Pb dating of zircon from the Xugou UHP eclogite, Sulu terrane, eastern China: International Geology Review, v. 47, p. 805–814. doi:10.2747/0020-6814.47.8.805.

Zhao, R., Zhang, R., Liou, J., Booth, A., Pope, E., and Chamberlain, C., 2007, Petrochemistry, oxygen isotopes and U-Pb SHRIMP geochronology of mafic–ultramafic bodies from the Sulu UHP terrane, China: Journal of Metamorphic Geology, v. 25, p. 207–224. doi:10.1111/j.1525-1314.2007.00691.x.

Zhao, X., Li, J., Ma, C., and Lang, Y., 2007a, Geochronology and geochemistry of the Gubei granodiorite, north Huaiyang: Implications for Mesozoic tectonic transition of the Dabie orogen: Acta Petrologica Sinica, v. 23, p. 1392–1402.

Zhao, Z.-F., Zheng, Y.-F., Chen, R.-X., Xia, Q.-X., and Wu, Y.-B., 2007b, Element mobility in mafic and felsic ultrahigh-pressure metamorphic rocks during continental collision: Geochimica Et Cosmochimica Acta, v. 71, p. 5244–5266. doi:10.1016/j.gca.2007.09.009.

Zhao, Z.-F., Zheng, Y.-F., Gao, T.-S., Wu, Y.-B., Chen, B., Chen, F.-K., and Wu, F.-Y., 2006b, Isotopic constraints on age and duration of fluid-assisted high-pressure eclogite-facies recrystallization during exhumation of deeply subducted continental crust in the Sulu orogen: Journal of Metamorphic Geology, v. 24, p. 687–702. doi:10.1111/j.1525-1314.2006.00662.x.

Zheng, Y.-F., Chen, R.-X., and Zhao, Z.-F., 2009, Chemical geodynamics of continental subduction-zone metamorphism: Insights from studies of the Chinese Continental Scientific Drilling (CCSD) core samples: Tectonophysics, v. 475, p. 327–358. doi:10.1016/j.tecto.2008.09.014.

Zheng, Y.-F., Fu, B., Gong, B., and Li, L., 2003, Stable isotope geochemistry of ultrahigh pressure metamorphic rocks from the Dabie–Sulu orogen in China: Implications for geodynamics and fluid regime: Earth-Science Reviews, v. 62, p. 105–161. doi:10.1016/S0012-8252(02)00133-2.

Zheng, Y.-F., Wu, Y.-B., Zhao, Z.-F., Zhang, S.-B., Xu, P., and Wu, F.-Y., 2005, Metamorphic effect on zircon Lu–Hf and U–Pb isotope systems in ultrahigh-pressure eclogite-facies metagranite and metabasite: Earth and Planetary Science Letters, v. 240, p. 378–400. doi:10.1016/j.epsl.2005.09.025.

Zhu, G., Liu, G.S., Niu, M.L., Xie, C.L., Wang, Y.S., and Xiang, B., 2009, Syn-collisional transform faulting of the Tan-Lu fault zone, East China: International Journal of Earth Sciences, v. 98, p. 135–155. doi:10.1007/s00531-007-0225-8.